جامعة بيرزيت

BIRZEIT UNIVERSITY

Faculty of Engineering and Technology

Joint Master Program in Electrical Engineering (JMEE)

Estimation of Angle of Arrival for Wireless Network System with Assisted Reconfigurable Intelligent Surface

Student name : Eng. Ayat Yassin

Supervisors : Dr. Ashraf Al-Rimawi

: Dr. Wael Al-Hashlamon

This Thesis is submitted in partial fulfillment of the Requtrements for the Master Degree in Electrical Engineering

July 13, 2023

BIRZEIT UNIVERSITY

Estimation of Angle of Arrival for Wireless Network System
with Assisted Reconfigurable Intelligent Surface

تقدير زاوية الوصول في نظام شبكة لاسلكية بمساعدة السطح الذكي القابل لإعادة التكوين

Submitted by:

Ayat Hani Yassin

<u>Approved by the Examining Committee</u>

Supervisors

Dr. Ashraf Al-Rimawi …………………………………….

Dr. Wael Al-Hashlamon ……………………………..

Examiners

Dr. Mohammad Jubran … ……………………………….

Dr. Qadri Mayaleh… ………………………………..

BIRZEIT, PALESTINE
July 2023

Declaration of Authorship

I declare that this thesis entitled " Estimation of Angle of Arrival for Wireless Network System with Assisted Reconfigurable Intelligent Surface " is the result of my own research except as cited in the references. It was submitted to the master's degree in Electrical Engineering from the Faculty of Engineering and Technology at Birzeit University, Palestine. The thesis has not been accepted for any degree and is not concurrently submitted in the candidature of any other degree.

Signed: Ayat Yassin
 Date: July 3, 2023

Abstract

In recent times, the reconfigurable intelligent surface (RIS) has emerged as a promising technology for improving network coverage and maintaining connectivity in the millimeter-wave (mmWave) communications channel. RIS acts as an intelligent mirror that interacts with incoming signals and reflects them toward the receiver regardless of location. In this thesis, we aim to optimize the Angle of Arrival (AoA) estimation of the received signal at the mobile station in a RIS-assisted communication system over Rayleigh fading channels using the Multiple Signal Classification (MUSIC) and MIN-NORM algorithms to enhance the strength of the received signal at the receiver in Non-Line-of-Sight (NLoS) paths. Additionally, the study aims to evaluate the impact of various factors on the accuracy of AoA estimation, including Signal-to-Noise Ratio (SNR), the number of RIS elements, the number of antenna array elements at the mobile station (MS), the number of snapshots, the location of RIS, and the Inter-element spacing in the antenna array on the estimation accuracy of the angle of arrival. The results of this study can provide insight into the behavior of MUSIC and MIN-NORM algorithms with varying these parameters. Finally, we will use simulation and analytical models to verify our system's performance.

المستخلص

ظهر السطح الذكي القابل لإعادة التكوين (RIS) مؤخرًا كتقنية واعدة لتحسين تغطية شبكات الجيل الخامس وما بعدها والحفاظ على الاتصال في قناة اتصالات الموجة المليمترية. يعمل السطح الذكي القابل لإعادة التكوين كمرآة ذكية تتفاعل مع الإشارات الواردة وتعكسها في اتجاه المستقبل بغض النظر عن موقعه. كما أن هذه التقنية منخفضة التكلفة وبسيطة التركيب مقارنة بغيرها من التقنيات الموجودة حاليا في شبكات وأنظمة الاتصالات اللاسلكية. وما يميّز هذه التقنية هو قدرتها على تحسين خصائص قناة الاتصال بين المُرسل والمُستقبل من خلال تعويض الأثر السلبي الناتج عن إزاحة الطور التي تسببها القناة في الإشارة المرسلة، حيث تُعد هذه الميزة حديثة ومُتطورة جدًا من حيث قدرتها على التحكم في قناة الاتصال نفسها، بينما جميع ما تم استخدامه سابقًا من التقنيات، تمتلك المقدرة فقط على تحسين أداء أنظمة الاتصال من خلال التحكم بخصائص المُرسل والمُستقبل على فرض بأن خصائص قناة الاتصال لا يمكن التحكم بها، وهذا ما تم دحضه مؤخرًا من خلال تقنية السطح الذكي القابل لإعادة التكوين.

في هذه الأطروحة، نهدف إلى تقدير زاوية الوصول للإشارة المستقبلة في المحطة المتنقلة في نظام اتصالات مدعوم بالسطح الذكي القابل لإعادة التكوين باستخدام خوارزمية تصنيف الإشارات المتعددة (MUSIC) و خوارزمية (MIN-NORM). أيضا، نهدف إلى تقييم تأثير العوامل المختلفة على دقة تقدير زاوية الوصول للإشارة المستقبلة، بما في ذلك نسبة الاشارة إلى الضوضاء، وعدد العناصر العاكسة على السطح الذكي، وعدد الهوائيات في المحطة المتنقلة، عدد العينات، وموقع السطح الذكي بالنسبة لمحطة القاعدة والتباعد بين العناصر في صفيف الهوائي. يمكن أن توفر نتائج هذه الدراسة نظرة ثاقبة لسلوك الخوارزميتين مع اختلاف هذه المعلمات.

Acknowledgements

Contents

List of Figures

List of Tables

List of Abbreviations

RIS	Reconfigurable Intelligent Surface
mmWave	millimeter Wave
AoA	Angle of Arrival
DoA	Direction of Arrival
AoD	Angle of Departure
DoD	Direction of Departure
MUSIC	Multiple Signal Classification
NLoS	Non Line of Sight
LoS	Line of Sight
MS	Mobile Station
5G	Fifth Generation
6G	sixth Generation
MIMO	Multiple Input Multiple Output
SIMO	Single Input Multiple Output
SNR	Signal to Noise Ratio
ULA	uniform Linear Array Antenna
UPA	uniform planar array
BS	Base Station
IRS	Intelligent Reconfigurable Surface
LIS	Large Intelligent Surface
AWGN	Additive White Gaussian Noise
EVD	Eigenvalue Decomposition
PMU	Pseudospectrum using MUSIC Algorithm
P_r	Power Received
P_t	Transmitted Power
CLT	Central Limit Theorem
RMSE	Root Mean Square Error
f_c	Carrier Frequency
GHz	Gigahertz
ESPRIT	Estimation of Signal Parameters via the Rotational Invariance Techniques
E_N	Noise Subspace
E_s	Signal Subspace
PL_F	Free-Space Path Loss

List of Symbols

λ	Wavelength for the Carrier Frequency
η	Path Loss Exponent
d	Inter-Element Spacing in the Array
Nr	Number of Array Elements at RIS
Nm	Number of Array Elements at MS
T	Number of Snapshots or Samples
K	Number of Sources Signal
No	Power of AWGN

List of Operations

$(.)^{H}$	Hermitian operator.

1 Introduction

For each new generation of cellular networks, there is an enormous increase in data rates due to rising demand and the introduction of innovative active use cases driven by emerging applications and supporting ecosystems. In 6G networks, some of these use cases include driverless and e-health. As a result, engineers and researchers must come up with new ideas to help them reach their goals during the concept-to-deployment cycle. 5G systems aim to use advanced technologies such as massive multiple-input multiple-output (MIMO) and mmWave communications for higher data rates, improved spectral efficiency, and increased frequency reuse. Massive MIMO enables beamforming in desired directions, while mmWave communication offers higher bandwidths, further improving achievable data rates and making smaller cells possibly due to the rapid attenuation of signals. A critical disadvantage of mmWave technology is its limited coverage and range. As a result, mmWave cannot propagate over long distances and is highly sensitive to physical obstructions such as walls and trees. Additionally, the Line-of-Sight (LOS) link is often blocked or weak, leading to frequent disconnections and reducing system reliability. Therefore, future generations propose using modern technology called RISs (Reconfigurable Intelligent Surfaces) in wireless networks to maintain a robust level of connectivity. They consist of reconfigurable reflectors that can easily adjust the delay and phase of incoming signals, making them well-suited for NLoS scenarios where the Los path is either blocked or has low signal strength. With the help of RISs, signal loss due to environmental obstacles can be compensated for, allowing for more reliable and efficient wireless networks .

The development of wireless communication has been focused primarily on creating transmitters and receivers that could successfully transmit signals over a difficult wireless channel until now. Now, advancements in signal processing are allowing us to shape the wireless channel to our own needs, breaking free from the limits of previous devices. We aim to study how we can benefit from the RIS to improve the estimation of the angle of arrival of the received signal at the mobile station. Therefore, high-resolution angle-of-arrival estimation is crucial for proper beam alignment to take advantage of the large beamforming gain.

2 Problem Formulation

2.1 Description

In this thesis, we consider the scenario wherein a mobile station equipped with a uniform linear array antenna (ULA) consisting of Nm antenna elements receive signals from a base station (BS) via a RIS consisting of Nr reflector elements, as illustrated in Fig. 1.
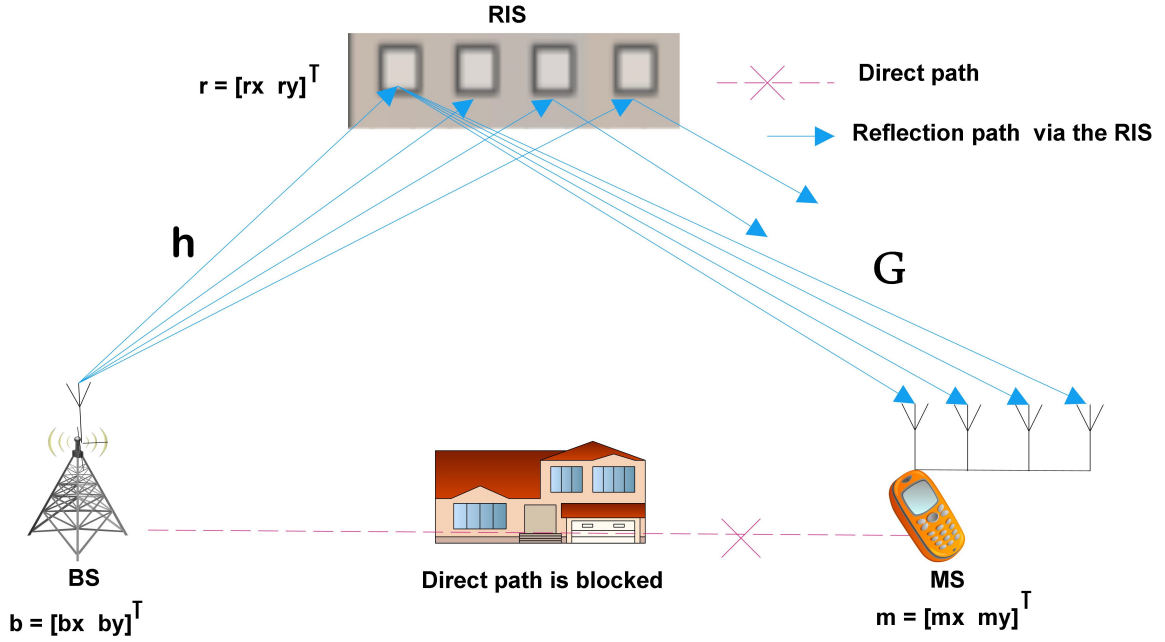
Figure 1: A RIS - assisted communication system.

The signal transmitted by the BS impinges on the RIS and is then reflected from each element of the RIS with an adjustable phase shift towards the mobile station in a specific direction. Our objective is to utilize reconfigurable intelligent surfaces to assist the base station in estimating the angle of arrival that provides maximum received power at the mobile station over Rayleigh fading channels. This will be achieved by employing the MUSIC and MIN-NORM algorithms. Additionally, we will assess the impact of various factors on optimizing the accuracy of the angle of arrival estimation. These factors include the number of array elements at both the mobile station and RIS, the number of signal snapshots, the enhancement of the SNR, the inter-element spacing of the antenna array, and the positioning of the RIS relative to the base station.

2.2   Motivation

We are aiming to use RISs to improve wireless communication networks. We are interested in realizing a controllable radio environment by adjusting the phase shift values of the RIS units through software. Our primary focus is to analyze the effect of RISs on the accurate detection of the angle of arrival of the received signal at the MS. The angle of arrival estimation is important for beamforming, tracking, and localization. By leveraging RISs, we aim to optimize the angle of the arrival estimation process and provide improved signal quality at the MS.

2.3   Main Contribution

Our primary focus is to leverage modern technology, specifically reconfigurable intelligent surfaces, to enhance the estimation of the angle of arrival of the mmWave received signal at the mobile station. This improvement enables proper beam alignment from the base station toward the receiver in the estimated direction, which is essential for maximizing beamforming gain. Although the MUSIC and MIN-NORM algorithms have been commonly utilized for the angle of arrival estimation in MIMO systems, their application in RIS-assisted communication systems has not been used.

3   Related Work

This section will provide a general overview of the RIS, which is deployed to maintain connectivity between the base station and the mobile station. Following that, we will present an overview of the algorithms used for estimating the angle of arrival.

3.1   Overview of Reconfigurable Intelligent Surface

Recently, the concept of RIS or intelligent reconfigurable surface (IRS), large intelligent surface (LIS) has been proposed to maintain connectivity and improve the network coverage and data rate in mmWave MIMO communications [3–7]. These surfaces are comprised of a large number of passive elements, referred to as meta-material units, which interact with the incident signals by intelligently reflecting them, thus improving the wireless system performance. A RIS can be viewed as a Software Defined Surface (SDS) that programs radio waves. It intentionally controls the propagation environment to enhance the signal quality at the receiver. The RIS can act as a clever reflector, enabling control of the propagation environment by adjusting the phase shifts, regardless of the receiver's location [8]. RISs have been used for a variety of goals in the literature, such as improved energy efficiency [6], security [9], spectral efficiency (SE) [10, 11], and even positioning [12, 13]. They are seen as an essential component of the development of beyond-5G wireless networks and enabling technologies to [4] , [6], [14, 15].

In order to adjust the phase shifts of RIS, some prior works [14–17], have assumed that the base station can accurately or roughly know the channels between the RIS and the transmitters/receivers. Furthermore, RIS elements can be implemented using phase shifters that reflect incident signals using two approaches for designing the RIS reflection matrix. The first approach requires channel estimation to design the reflection matrix, which results in massive channel training overhead; the second approach selects the RIS reflection matrix from quantized codebooks via online beam/reflection training, but the size of the reflection codebooks needs to be in the order of the number of antennas, which results in tremendous training costs. A hybrid analog/digital architecture at the RIS may be employed to avoid this massive training with channel estimation strategies used to obtain the channels.

Recently, numerous research works have studied the performance of RIS-assisted wireless systems. The authors in [18] studied the effect of the number of reflecting elements in bidirectional full-duplex (FD) wireless communication systems with the support of RISs. Results showed that the performance of the system was significantly dependent on the total number of reflecting elements in the RISs. In particular, when the total number of reflecting elements increased continuously, the outage probability (OP) decreased continuously. However, when the total number of reflecting elements was already large enough, the OP decreased greatly. To improve the performance of the considered RIS-FD system, we could use a larger number of reflecting

elements with one RIS or multiple RISs. In [19], the author studied the coverage of a downlink RIS-assisted network, which comprised one base station and one user. The analysis revealed that the orientation of the RIS as well as the horizontal distance between the RIS and the base station had a significant impact on cell coverage. The results showed that when the RIS moved away from the base station, the coverage initially increased. However, if the distance between the RIS and base station continued to increase, the cell coverage degraded due to the decreased SNR received. Consequently, it is important to position the RIS at a moderate distance from the base station to ensure optimum coverage. In [20], the authors investigated coverage, the delay outage rate, and the probability of the received SNR gain in a RIS-assisted communication system over a Rayleigh fading channel with the use of the Central Limit Theorem (CLT). Meanwhile, [21] analyzed the ergodic capacity (EC). In [22], the authors minimized the outage probability by optimizing the phase shifts of a RIS over Rician fading channels. Additionally, [23] studied the impact of phase noise on the bit error rate (BER) over the Rayleigh fading channel. [24] quantified the effect of discrete phase shifts on the achievable rate over Rician fading channels. Moreover, [25] analyzed the effect of discrete phase shifts for achieving the entire diversity order over the Rayleigh fading channel. Finally, [26] proposed the distribution of SNR in multiple antennae RIS-assisted systems in the presence of phase noise in a general framework. Recently, many research papers have been published to consider situations where the LoS link is either weak or unavailable, so a RIS is used to reliably transmit data by optimizing the phase shifts of its reconfigurable elements and the precoding and decoding vectors at the transmitter and receiver, such as in [6], [11], [27–32]. Several designs have been proposed using RIS technology for a variety of advanced communication techniques, such as mm-wave communications [30], unmanned aerial vehicle (UAV) networks [33–35], and physical layer security [31].

3.2   Algorithms for estimating the angle of arrival

Standard antennas are designed to send and receive radio signals effectively. In contrast, smart antennas must also be able to estimate the direction of arrival (DoA) of the received signal and use this information for beamforming [36, 37]. DoA estimation is an important issue in smart antenna systems [38–40]. It is used in various wireless communication applications, such as sonar, navigation, electronic surveillance, radar, radio astronomy, tracking [41–43] and localization. DoA estimation is a process that determines the angle of arrival of a received signal by processing the signal impinging on an antenna array [44]. This process can help improve the quality of service in a communication system by focusing reception and transmission only in the estimated direction.

AoA estimation can be realized using algorithms classified as conventional and non-conventional approaches [45]. Conventional methods are called non-subspace methods, including Minimum

Variance Distortionless Response (MVDR) Estimator [46], Maximum Entropy Method (MEM) [8],Maximum Likelihood Method (MLM), Bartlett and capon [47] methods. Non- conventional methods are called subspace methods, including MUSIC [48–51], MIN-NORM Method (MNM) [52–54] and the estimation of signal parameters via the rotational invariance technique (ESPRIT) [55–57]. Conventional methods focus on determining a pseudo-spectrum at first, then AoAs are determined by searching for the power peaks in the utilized spectrum band. The Pseudo-spectrum relies on a mathematical function, which yields the best results when employed along with an accurate estimation method to calculate the pseudo-spectrum. Conventional methods strongly depend on the antenna array aperture's physical size since a small aperture may cause poor resolution and inaccurate signal detection. Moreover, they are useful for wireless environments where signal properties information is unknown. Subspace methods rely on decomposing the signal's covariance matrix into two orthogonal matrices: the signal subspace and the noise subspace. Estimating the direction of arrival is performed using the noise subspace, assuming that the noise in each channel is highly uncorrelated. Subspace methods have gained more popularity than conventional because they provide higher resolution than conventional algorithms [58, 59]. The estimation accuracy of subspace methods depends on several parameters [60], including the number of data samples, array elements, inter-element spacing, antenna type, and SNR. The author in [61] presents the angle of arrival estimation simulation, using the MUSIC and ESPRIT algorithms. The simulation results indicate that the MUSIC algorithm is more accurate and stable than the ESPRIT algorithm. As reported by the author felt in [59], the MUSIC method is a more widely-accepted parameter estimation algorithm than ESPRIT, wherein it can be leveraged both for uniform and non-uniform linear arrays. However, ESPRIT has relatively limited applications and is limited to some peculiar array structures [62]. In [63], the author presents the outcomes of using different techniques to evaluate the direction of arrival in the MIMO OFDM radar system. The four approaches evaluated were MVDR, MUSIC, MIN-NORM, and ESPRIT. The results of the simulation showed that the MUSIC algorithm gave the best resolution for determining the direction of arrival, followed by MIN-NORM and ESPRIT, while the MVDR give the worst resolution.

The ultimate goal is to study the performance of RIS to optimize the accurate estimation of the angle of arrival of the received signal at the mobile station. To achieve this, an algorithm belonging to the subspace, specifically the MUSIC algorithm, is utilized due to its classification of high performance and accuracy in estimating the direction of arrival. Additionally, another algorithm belonging to the subspace, MIN-NORM, has been selected to validate the results obtained from the MUSIC algorithm. Based on our knowledge of the literature, MUSIC, and MIN-NORM algorithms have been used in MIMO systems but have not been used in RIS-assisted communication systems.

4 Propagation and Fading

In this section, we will provide a general overview of the fading that the signal may experience during its transmission from the sender to the receiver.

Radio propagation in wireless communication occurs when radio waves move from a transmitter to a receiver and is affected by various physical phenomena, such as reflection, diffraction, and scattering [64]. Reflection occurs when an electromagnetic wave travels and encounters an object that is much larger than the wavelength, such as the surface of the Earth or a building, causing the signal power to be reflected back to where it originated from rather than continuing to its destination. Diffraction causes the waves to bend and spread out when they encounter a sharp irregular surface or small openings, creating secondary waves that can travel between a transmitter and receiver even when a direct, line-of-sight connection is not available. Scattering occurs when electromagnetic radiation is diverted off its straight path by objects that are small compared to the wavelength, such as street signs, lamp posts, and foliage. The transmission of a radio signal is an unpredictable and complex process, determined by reflection, diffraction, and scattering, the strength of which changes depending on the environment in different situations.

Wireless channels have a unique characteristic called fading, which is the changing of the signal's amplitude over time and frequency. This variation is unlike other sources of signal degradation, such as additive noise, as it is considered to be a non-additive disturbance to the wireless channel. Fading [65–67] be induced by multipath propagation, known as multipath fading, or caused by obstacles that affect a radio wave's propagation, known as shadow fading. Fading can be divided into two categories: large-scale and small-scale. Large-scale fading is caused by path loss of the signal over distance and due to shadowing caused by objects such as buildings over long distances. On the other hand, small-scale fading is caused by the constructive and destructive interference of multiple signal paths over short distances. This type of fading can be either fast or slow, depending on the Doppler spread and frequency selectivity.

4.1 Free space propagation model

The free-space propagation model is utilized to calculate the strength of the received signal in the LoS environment [64]. The received power, Pr, at the receiver, can be expressed by the Friis equation as:

$$Pr(d) = \frac{P_s.G_t.G_r.\lambda^2}{(4.\pi)^2.d^2.L} \tag{1}$$

where P_s is the transmit power (in watts), λ is the wavelength of the carrier frequency (in meters), d is the distance between the transmitter and the receiver (in meters), Gt and Gr

are the transmitting and receiving antenna gains, respectively, and L is the system loss factor which is independent of the propagation environment. The system loss factor represents overall attenuation or loss in the actual system hardware, including transmission line, filter, and antennas. In general, $L \geq 1$, but $L = 1$ if we assume that there is no loss in the system hardware. It is clear from Eqn.(1) that the received signal power decreases with increasing distance between the transmitter and receiver. The free-space path loss (PL$_F$) can be derived from Eqn.(1) as follows:

$$PL_F[dB] = 10log_{10}\left(\frac{Pt}{Pr}\right) = 10log_{10}\left(\frac{4^2.\pi^2.d^2}{G_r.G_t.\lambda^2}\right) \qquad (2)$$

Without antenna gains (i.e., $G_t = G_r = 1$), Equation (2) is reduced to

$$PL_F[dB] = 10log_{10}\left(\frac{Pt}{Pr}\right) = 20log_{10}\left(\frac{4.\pi.d}{\lambda}\right) \qquad (3)$$

A more generalized form of the path loss model can be constructed by modifying the free-space path loss with the path loss exponent η that varies with the environments. This is known as the log-distance path loss model, in which the path loss at distance d is given as

$$PL_{LD}(d)[dB] = PL_F(d_0) + 10\eta \quad log\left(\frac{d}{d_0}\right) \qquad (4)$$

where d_0 is a reference distance at which or closer to the path loss inherits the characteristics of free-space loss in Equation (2), and η is the path loss exponent ($\eta = 2$ corresponds to free space); it can vary from 2 to 6, depending on the propagation environment Path loss exponent is one of the most important parameters widely considered in wireless communication analysis to specify the propagation environment [68]. Typical values of the path loss exponent are shown in Table 1.

Table 1: Path loss exponent for different environments [2]

Environment	Path Loss Exponent, η
Free Space	2
Urban area cellular radio	2.7 to 3.5
Shadowed urban cellular radio	3 to 5
In building line-of-sight	1.6 to 1.8
Obstructed in buildings	4 to 6
Obstructed in factories	2 to 3

Meanwhile, the reference distance d_0 must be properly determined for different propagation environments. For example, d_0 is typically set as 1 km for a cellular system with a large coverage (e.g., a cellular system with a cell radius greater than 10 km). However, it could be 100 m or 1 m, respectively, for a macrocellular system with a cell radius of 1km or a microcellular system with an extremely small radius.

4.2   Statistical models for multipath fading channels

The wireless transmission environment can be either LoS or NLoS. The probability density function (PDF) of the received signal in NLoS follows the Rayleigh distribution, while in LoS, the PDF of the received signal follows the Rician distribution.

The received signal in a wireless channel propagation environment can be seen as the combination of signals from an infinite number of scatters. According to the central limit theorem, the received signal can be modeled as a Gaussian random variable.

4.2.1   Clarke's model

The received signal from flat fading channel consists of the superposition of a large number L_s of local uncorrelated scatterers that arrive at the receiver almost simultaneously with a common propagation delay. Each of these scatterers is characterized by its own random amplitude and random phase. Thus, the fading process can be modeled as a sum of L_s weighted complex exponentials [69]:

$$h(t) = \sum_{l=1}^{L_s} g_l e^{((j2\pi f_m cos\theta_l)t + \phi_l)} \tag{5}$$

L_s : number of scatterers.

g_l: random amplitude of the lth scatterer.

θ_l : random angle of arrival of the lth scatterer.

ϕ_l : random initial phase of the lth scatterer.

fm : maximum Doppler frequency (fm= v/ λ).

4.2.2   Rayleigh fading distribution

When there are a large number of scatterers, according to the central limit theorem, the fading process c(t) can be approximated as a complex Gaussian process [70], [64], [71]

$$c(t) = |c(t)|.e^{-j\vartheta(t)} \tag{6}$$

When no direct line-of-sight path exists between the transmitter and the receiver, the fading process c(t) will have zero-mean and variance of σ^2.

In that case: the envelope r= $|c(t)|$ has a Rayleigh probability density function:

$$
p(r) = \begin{cases} \frac{r}{\sigma^2} e^{\left(-\frac{r^2}{2\sigma^2}\right)} & r \geq 0 \\ \\ 0 & r < 0 \end{cases}
\tag{7}
$$

σ^2 : average power of the received faded signal.

$\vartheta(t)$ denotes the phase which is uniformly distributed over a 2π interval.

The probability that the envelope of the received signal does not exceed a specified value Q is given by the Cumulative Distribution Function (CDF):

$$
Pr(r \leq Q) = \int_0^Q p(r).dr = \int_0^Q \frac{r}{\sigma^2} exp\left(-\frac{r^2}{2\sigma^2}\right).dr = 1 - exp\left(-\frac{Q^2}{2\sigma^2}\right)
\tag{8}
$$

The mean value r_{mean} of the Rayleigh distribution is given by:

$$
r_{mean} = E[r] = \int_0^\infty r.p(r).dr = \sigma\sqrt{\frac{\pi}{2}} = 1.2533\sigma
\tag{9}
$$

The variance of the Rayleigh distribution is given by σ_r^2 :

$$
\sigma_r^2 = E[r^2] - (E[r])^2 = \int_0^\infty r^2.p(r).dr - \sigma^2\frac{\pi}{2} = \sigma^2\left(2 - \frac{\pi}{2}\right) = 0.4292\sigma^2
\tag{10}
$$

5   System Model

In this section, we will describe the scenario model, channel model, as well as the mathematical and geometric relationships.

5.1   Scenario

We are considering a single-input multiple-output (SIMO) wireless system, wherein a reconfigurable intelligent surface composed of Nr reflecting elements is deployed to assist in communication from the base station with a single antenna transmitter to the mobile station with an Nm antenna receiver, as illustrated in Fig. 2.
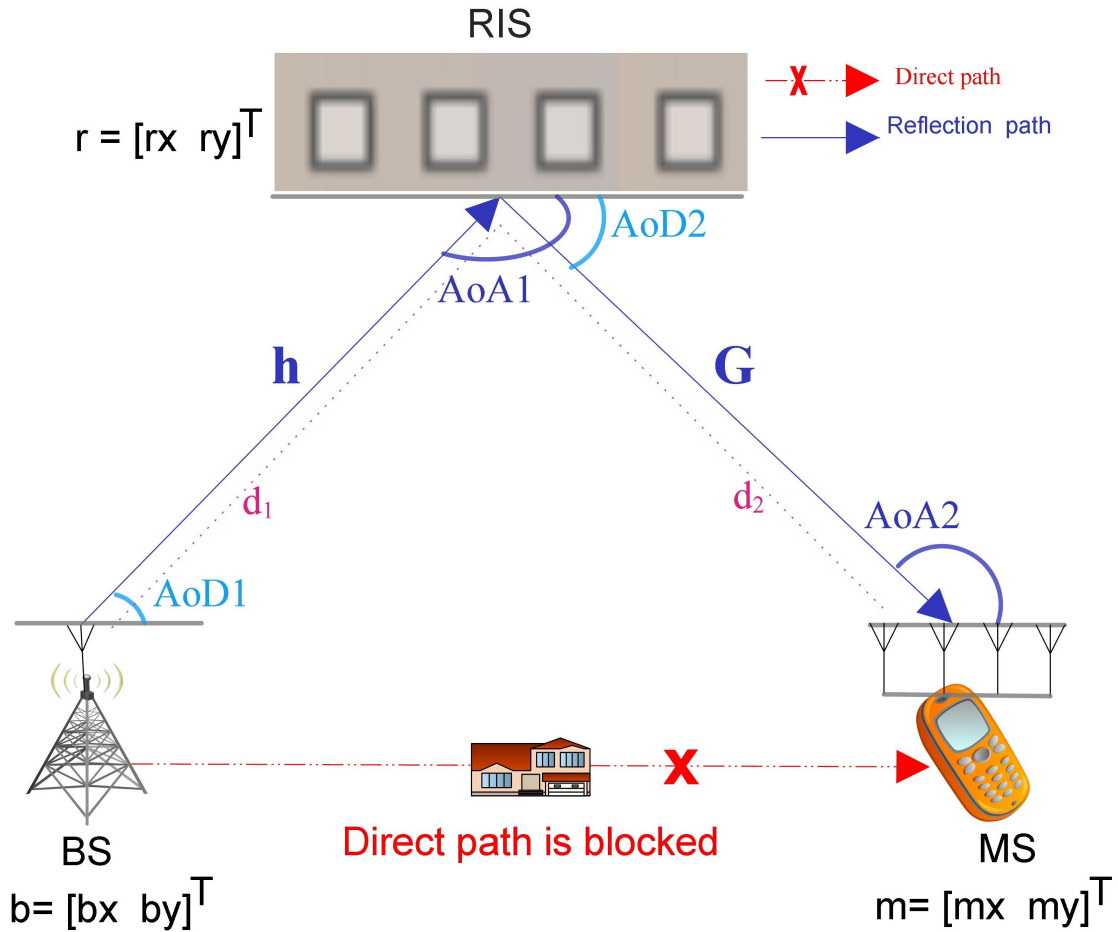
Figure 2:   The direction of departure and arrival of the signal in the system with the aid of a RIS, AoA2 is unknown and needs to be estimated.

We will assume that the RIS (i.e., phase shifters) has Nr passive reflecting elements arranged in a uniform array of reflectors. Also, we will assume the position of BS is known $\mathbf{b} = [b_x \quad b_y]^T$ and the position of RIS is known $\mathbf{r} = [r_x \quad r_y]^T$ while the position of MS is unknown $\mathbf{m} = [m_x \quad m_y]^T$. Additionally, we will assume the direct transmission path between BS and MS is blocked by

an obstacle, and the propagation channel between BS and MS is only composed of a reflection path via the RIS. We aim to estimate the angle of arrival of the received signal at the mobile station that gives the highest received power at the mobile station.

5.2   Channel model

The propagation channel via RIS is composed of two individual channels, the channel between BS and RIS, denoted by $\mathbf{h} \in \subset^{Nr \times 1}$ and the channel between RIS and MS, denoted by $\mathbf{G} \in \subset^{Nm \times Nr}$.

Furthermore, we will assume that all the channels are independent flat-fading with:

$$\mathbf{h} = \begin{bmatrix} h_1 \\ h_2 \\ h_{Nr} \end{bmatrix} \qquad \mathbf{h} \in \subset^{Nr \times 1} \tag{11}$$

To further explain $\mathbf{h}$, we can rewrite it as follows:

$$\mathbf{h} : h_i = \left(\frac{\lambda}{4\pi d_1^{\eta/2}} \right) \alpha e^{j\phi_i} \qquad i = 1, 2, ..., Nr.$$

$$= \left(\frac{\lambda}{4\pi d_1^{\eta/2}} \right) |\alpha| e^{jF} e^{j\phi_i} \tag{12}$$

$$= \left(\frac{\lambda}{4\pi d_1^{\eta/2}} \right) |\alpha| e^{j(F+\phi_i)}$$

Where h_i denotes fading channel between the BS and the i-th reflecting meta-surface of the RIS, $\lambda/(4\pi d_1^{\eta/2})$ is the free-space path loss that occurred in the link between the BS and the RIS,λ denotes the wavelength of the carrier frequency, d_1 is the distance between BS and RIS, η is the path loss exponent, $\alpha = |\alpha| e^{jF}$ with $| \alpha |$ and F denoting the modulus and phase of the complex gain α over the BS-RIS path and follows the Rayleigh distribution, the elements of α an i.i.d in the Gaussian distribution CN$\sim (0, 1)$, ϕ_i is the phase shift induced by the element i at the RIS, as illustrated in Fig. 3 and Appendix A.

$$\phi_i = -2\pi(i-1)\frac{d}{\lambda}cos(AoA1) \quad \phi_i \in [-\pi, \pi] \tag{13}$$

AoA1 denotes the angle of arrival or direction of arrival of the received signal at the RIS from the BS and is defined at the RIS relative to the horizontal direction, as illustrated in Fig. 2.

The antenna array response and steering vector at the RIS are denoted as

$$\mathbf{h} = \left(\frac{\lambda}{4\pi d_1^{\eta/2}}\right)|\alpha| \begin{bmatrix} e^{jF} \\ \\ e^{j(F-2\pi\frac{d}{\lambda}cos(AoA1))} \\ \\ e^{j(F-2\pi(Nr-1)\frac{d}{\lambda}cos(AoA1))} \end{bmatrix} \tag{14}$$

Figure 3: Phase shift induced by each element in ULA at RIS and MS.

The channel $\mathbf{G} \in \subset^{Nm \times Nr}$ from RIS to MS is:

$$\mathbf{G} = \left(\frac{\lambda}{4\pi d_2^{\eta/2}}\right)\mathbf{zg} \tag{15}$$

$\lambda/(4\pi d_2^{\eta/2})$ is the free-space path loss that occurred in the link between the RIS and the MS, where d_2 is the distance between the RIS and the MS.

The receiving steering vector at the MS from the RIS for the link between the RIS and the MS is denoted by $\mathbf{z}$, and the transmitting steering vector from the RIS toward the MS is denoted by $\mathbf{g}$.

$$\mathbf{z} = \begin{bmatrix} z_1 \\ z_2 \\ z_{Nm} \end{bmatrix} \qquad \mathbf{z} \in \subset^{Nm \times 1} \tag{16}$$

To further explain $\mathbf{z}$, we can rewrite it as follow:

$$\mathbf{z} : z_k = \rho.e^{j\varphi_k} \qquad for \quad k = 1, 2, ..., Nm.$$

$$= \mid \rho \mid e^{jR} e^{j\varphi_k} \tag{17}$$

$$= \mid \rho \mid e^{j(R+\varphi_k)}$$

Where, z_k denotes the channel coefficient between the RIS and MS for the kth antenna at the MS (where $k = 1, 2, \ldots, N_m$), $\rho = \mid \rho \mid e^{jR}$ with $\mid \rho \mid$ and R denoting the magnitude and phase of the complex gain ρ over the RIS-MS path and follows the Rayleigh distribution, the elements of ρ are i.i.d in the Gaussian distribution $\mathcal{CN} \sim (0, 1)$, and φ_k is the phase shift induced by element k of MS, as illustrated in Fig. 3 and Appendix B.

$$\varphi_k = -2\pi(k-1)\frac{d}{\lambda}\cos(\text{AoA2}), \qquad \varphi_k \in [-\pi, \pi] \tag{18}$$

AoA2 denotes the AoA or DoA of the received signal at the MS from the RIS and is defined at the MS relative to the horizontal direction, as illustrated in Fig. 2.

The steering vector at the MS is denoted as follows:

$$\mathbf{z} = |\rho|. \begin{bmatrix} e^{jR} \\ e^{j(R-2\pi\frac{d}{\lambda}cos(AoA2))} \\ e^{j(R-2\pi(Nm-1)\frac{d}{\lambda}cos(AoA2))} \end{bmatrix} \tag{19}$$

$$\mathbf{g} = \begin{bmatrix} g_1 & g_2 & g_{Nr} \end{bmatrix} \qquad \mathbf{g} \in \subset^{1 \times Nr} \tag{20}$$

To further explain $\mathbf{g}$, we can rewrite it as follow:

$$\mathbf{g} : g_i = \beta e^{j\theta_i} \qquad for \quad i = 1, 2, ..., Nr.$$

$$= \mid \beta \mid e^{jb} e^{j\theta_i} \tag{21}$$

$$= \mid \beta \mid e^{j(b+\theta_i)}$$

Where, g_i is the channel coefficient between the RIS and the MS for the i-th reflecting meta-surface (i = 1, 2, ..., Nr), $\beta = \mid \beta \mid e^{jb}$ $with$ $\mid \beta \mid$ and b denoting the magnitude and phase of the complex gain β over the RIS-MS path and follows the Rayleigh distribution, the elements of β are i.i.d in the Gaussian distribution $\mathcal{CN} \sim (0,1)$, and θ_i is the phase shift induced by the element i of RIS and denotes the direction of the departure signal from RIS toward MS, as illustrated in Fig. 3 and Appendix c.

$$\theta_i = -2\pi(i-1)\frac{d}{\lambda}\cos(\text{AoD2}), \qquad \theta_i \in [-\pi, \pi] \tag{22}$$

AoD2 denotes the angle of departure (AoD) or direction of departure (DoD) of the transmitted signal from the RIS to the MS and is defined at the RIS relative to the horizontal direction, as illustrated in Fig. 2.

The steering vector from the RIS is denoted as follows:-

$$\mathbf{g} = |\beta| \begin{bmatrix} e^{jb} & e^{j(b-2\pi\frac{d}{\lambda}cos(AoD2))} & e^{j(b-2\pi(Nr-1)\frac{d}{\lambda}cos(AoD2))} \end{bmatrix} \tag{23}$$

to write $\mathbf{G}$ with new expression

$$\mathbf{G} = \left(\frac{\lambda}{4\pi d_2^{\eta/2}}\right) \mid \rho \mid . \mid \beta \mid \begin{bmatrix} e^{jR} \\ e^{j(R-2\pi\frac{d}{\lambda}cos(AoA2))} \\ e^{j(R-2\pi(Nm-1)\frac{d}{\lambda}cos(AoA2))} \end{bmatrix} \begin{bmatrix} e^{jb} & e^{j(b-2\pi\frac{d}{\lambda}cos(AoD2))} & e^{j(b-2\pi(Nr-1)\frac{d}{\lambda}cos(AoD2))} \end{bmatrix}$$
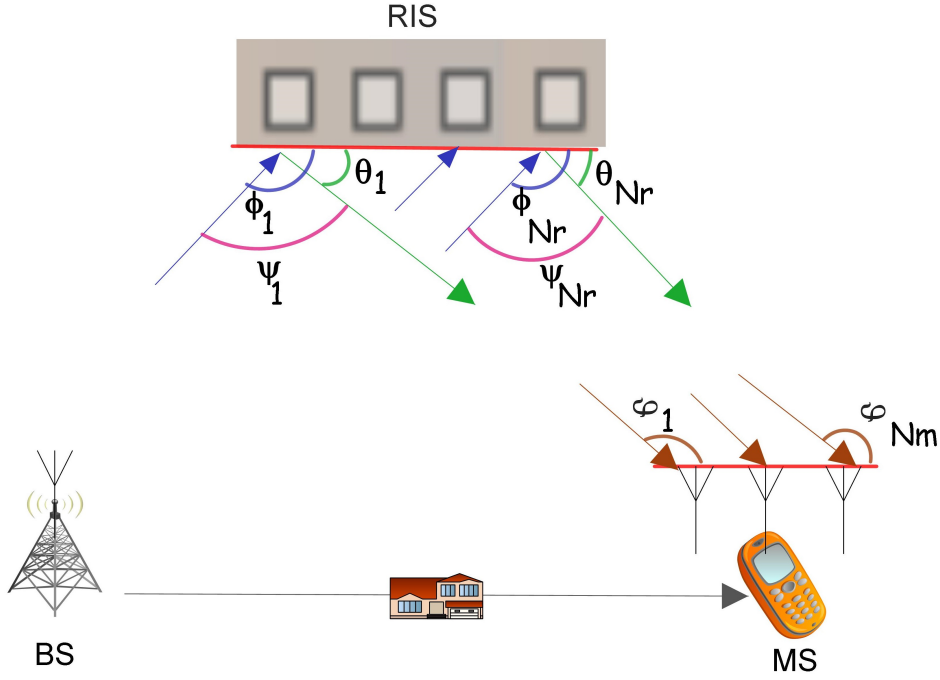
Each unit of the RIS reflects the received signal from the BS independently with an adjustable phase shift. We model the reflection by the units of the RIS using

$$\mathbf{q} = \begin{bmatrix} q_1 \\ q_2 \\ q_{Nr} \end{bmatrix} \qquad \mathbf{q} \in \mathbb{C}^{Nr \times 1} \tag{24}$$

$$\mathbf{q} : q_i = \Gamma_i e^{j\psi_i}, \qquad \psi_i \in [-\pi, \pi], \quad \Gamma_i \in [0, 1] \tag{25}$$

ψ_i and Γ_i denote the phase shift and amplitude reflection coefficient of the i-th unit, respectively. For simplicity, we set $\Gamma_i = 1$, $\forall i$.

In [72], the author mentioned that the maximum SNR of the received signal at the receiver is achieved when the RIS phase shift matches the combined phase of the user to the RIS channel and the RIS to BS channel. Based on that, the optimal choice of the phase shift of each reflector element on the RIS to maximize the received signal at the MS is equal to

$$\psi_i + \angle g_i + \angle h_i = 0 \tag{26}$$

$$\begin{aligned}
\psi_i &= -\left(\angle g_i + \angle h_i \right) \\
&= -[(b + \theta_i) + (F + \phi_i)] \\
&= -[(b - \frac{2\pi.(i-1)d.cos(AoD2)}{\lambda}) + (F - \frac{2\pi.(i-1)d.cos(AoA1)}{\lambda})]
\end{aligned} \tag{27}$$

to write $\mathbf{q}$ with new expression:-

$$\mathbf{q} = \begin{bmatrix} e^{-j(b+F)} \\ e^{-j(b - \frac{2\pi dcos(AoD2)}{\lambda} + F - \frac{2\pi dcos(AoA1)}{\lambda})} \\ e^{-j(b - \frac{2\pi(Nr-1)dcos(AoD2)}{\lambda} + F - \frac{2\pi(Nr-1)dcos(AoA1)}{\lambda})} \end{bmatrix} \tag{28}$$

The entire channel between the BS and the MS via RIS $\in \mathbb{C}^{Nm \times 1}$ can be formulated as:-

$$\mathbf{h}_{total} = \mathbf{G}\Phi\mathbf{h} \tag{29}$$

Where $\Phi = diag(\mathbf{q}) \in \mathbb{C}^{Nr \times Nr}$ is the phase control matrix at the RIS and denotes a diagonal matrix whose diagonal elements are the corresponding elements of the $\mathbf{q}$. It is diagonal because each RIS element reflects the signal independently, and there is no signal coupling or joint

16

processing over the RIS elements [73–76].

We only consider signals reflected by the RIS for the first time and ignore those reflected by it twice to reduce the effect of path loss. Hence, the received signal reflected from all RIS elements $\mathbf{y} \in \mathbb{C}^{Nm \times 1}$ can be modeled as a superposition of their respective reflected signals as follow:

$$\mathbf{y} = \sqrt{P_s}(\mathbf{G}\Phi\mathbf{h})s + \mathbf{n} \tag{30}$$

P_s is the transmit power at the BS, s is the transmitted pilot signal, and $\mathbf{n} \in \mathbb{C}^{Nm \times 1}$ is the additive white Gaussian noise (AWGN) n$\sim \mathcal{CN}(0, No)$.

Notification:

The equations mentioned in the system model assume the transmission of a single sample. Our goal is to transmit multiple samples from the signal. The general form of the received signal at the mobile station after sending T samples is shown in Equation (31).

$$\mathbf{y}_T = \sqrt{P_s}(\mathbf{G}_T\Phi_T\mathbf{h}_T)s_T + \mathbf{n}_T \qquad \mathbf{y}_T \in \mathbb{C}^{Nm \times T}$$

$$\tag{31}$$

$$= \sqrt{P_s}(\mathbf{h}_{TOTAL})s_T + \mathbf{n}_T$$

Where, $s_T \in \mathbb{C}^{1 \times T}$ denotes T samples transmitted, $\mathbf{h}_{TOTAL} = (\mathbf{G}_T\Phi_T\mathbf{h}_T)$ denotes the entire channel between the BS and the MS via RIS $\in \mathbb{C}^{Nm \times T}$, and $\mathbf{n}_T \in \mathbb{C}^{Nm \times T}$ is AWGN at the MS $\mathbf{n}_T \sim \mathcal{CN}(0, N0)$.

$\mathbf{h}_T \in \mathbb{C}^{Nr \times T}$ indicate the channel between BS and RIS for the T samples, which can be represented as:

$$\mathbf{h}_T = \left(\frac{\lambda}{4\pi d_1^{\eta/2}}\right) \begin{bmatrix} e^{j\phi_1} \\ e^{j\phi_2} \\ e^{j\phi_{Nr}} \end{bmatrix} \begin{bmatrix} \alpha_1 & \alpha_2 & \alpha_T \end{bmatrix} \tag{32}$$

$$= \left(\frac{\lambda}{4\pi d_1^{\eta/2}}\right) \begin{bmatrix} 1 \\ e^{-j2\pi\frac{d}{\lambda}cos(AoA1)} \\ e^{-j2\pi(Nr-1)\frac{d}{\lambda}cos(AoA1)} \end{bmatrix} \begin{bmatrix} \alpha_1 & \alpha_2 & \alpha_T \end{bmatrix}$$

$\alpha_1 = |\alpha_1|.e^{jF_1}$ with $|\alpha_1|$ and F_1 denoting the modulus and phase of the complex gain α_1 over the BS-RIS path when sending sample 1 and follows the Rayleigh distribution.

$\mathbf{G}_T$ indicates the channel between the RIS and MS for the T samples, which can be represented as:

$$\mathbf{G}_T = \left(\frac{\lambda}{4\pi d_2^{\eta/2}}\right) \mathbf{z}_T \mathbf{g}_T \qquad\qquad \mathbf{G}_T \in \subset^{Nm \times Nr} \qquad (33)$$

$$\mathbf{z}_T = \begin{bmatrix} e^{j\varphi_1} \\ e^{j\varphi_2} \\ e^{j\varphi_{Nm}} \end{bmatrix} \begin{bmatrix} \rho_1 & \rho_2 & \rho_T \end{bmatrix} \qquad \mathbf{z}_T \in \subset^{Nm \times T} \qquad (34)$$

$$= \begin{bmatrix} 1 \\ e^{-j2\pi \frac{d}{\lambda} cos(AoA2)} \\ e^{-j2\pi(Nm-1)\frac{d}{\lambda} cos(AoA2)} \end{bmatrix} \begin{bmatrix} \rho_1 & \rho_2 & \rho_T \end{bmatrix}$$

$$\mathbf{g}_T = \begin{bmatrix} \beta_1 \\ \beta_2 \\ \beta_T \end{bmatrix} \begin{bmatrix} e^{j\theta_1} & e^{j\theta_2} & e^{j\theta_{Nr}} \end{bmatrix} \qquad \mathbf{g}_T \in \subset^{T \times Nr} \qquad (35)$$

$$= \begin{bmatrix} \beta_1 \\ \beta_2 \\ \beta_T \end{bmatrix} \begin{bmatrix} 1 & e^{-j2\pi \frac{d}{\lambda} cos(AoD2)} & e^{-j2\pi(Nr-1)\frac{d}{\lambda} cos(AoD2)} \end{bmatrix}$$

β_1 is represented as $\mid \beta_1 \mid e^{jb_1}$, where $\mid \beta_1 \mid$ and b_1 denote the magnitude and phase, respectively, of the complex gain β_1 over the RIS-MS path when sending sample 1, and it follows the Rayleigh distribution.

Similarly, ρ_1 is represented as $\mid \rho_1 \mid e^{jR_1}$ where $\mid \rho_1 \mid$ and R_1 denoting the magnitude and phase, respectively, of the complex gain ρ_1 over the RIS-MS path when sending sample 1, and it follows the Rayleigh distribution.

$$\Phi_T = [diag(\mathbf{q_1}) \quad diag(\mathbf{q_2}) \quad diag(\mathbf{q_T})] \quad \in \subset^{Nr \times Nr*T} \tag{36}$$

where $diag(\mathbf{q_1})$ is the phase control matrix at the RIS when sending sample one.

$$\mathbf{q_1} = \begin{bmatrix} e^{-j(b_1+F_1)} \\ \\ e^{-j(b_1 - \frac{2\pi dcos(AoD2)}{\lambda} + F_1 - \frac{2\pi dcos(AoA1)}{\lambda})} \\ \\ e^{-j(b_1 - \frac{2\pi(Nr-1)dcos(AoD2)}{\lambda} + F_1 - \frac{2\pi(Nr-1)dcos(AoA1)}{\lambda})} \end{bmatrix} \tag{37}$$

The received signal strength indicator (RSSI) measures the strength of the signal at the receiver, with higher RSSI values indicating a stronger signal. Mathematically, the received signal strength at the receiver can be expressed as follows:

$$P_r = (P_s).|\mathbf{G}_T \Phi_T \mathbf{h}_T|^2 \tag{38}$$

$$P_r(dBm) = 10log_{10}\left(\frac{P_s.|\mathbf{G}_T \Phi_T \mathbf{h}_T|^2}{1mW}\right) \tag{39}$$

In various communication systems, the SNR is one of the parameters used to measure the quality of the communication link. Higher SNR values indicate better communication link quality. Mathematically, it is expressed as follows:

$$SNR = \frac{P_r}{P_n} = \frac{(P_s).|\mathbf{G}_T \Phi_T \mathbf{h}_T|^2}{No} \tag{40}$$

$$SNR(dB) = 10log_{10}\left(\frac{(P_s).|\mathbf{G}_T \Phi_T \mathbf{h}_T|^2}{No}\right) \tag{41}$$

5.3 Mathematical and geometric relationships

Based on our assumption, the position of the RIS is known to the BS. Therefore, AoD1 and AoA1 are known. The information on AoD2 and AoA2 is unknown, and we will estimate these parameters. Based on Fig. 2, we can impose the following geometric relationships among the BS, RIS, and MS as follows:-

$$AoD1 = tan^{-1}\left(\frac{r_y - b_y}{r_x - b_x}\right) \qquad AoD1 \in (0, 90) \qquad (42)$$

$$AoA1 = -180 + AoD1 \qquad AoA1 \in (-180, 0) \qquad (43)$$

$$AoD2 = -cos^{-1}\left(\frac{m_x - r_x}{\sqrt{(r_x - m_x)^2 + (r_y - m_y)^2}}\right) \quad AoD2 \in (-180, 0) \qquad (44)$$

$$AoA2 = 180 + AoD2 \qquad AoA2 \in (0, 180) \qquad (45)$$

To determine the accuracy of the angle of arrival estimation, we can calculate the root mean square error (RMSE) of the angle of arrival estimation. RMSE should be small for accurate estimation.

$$RMSE = \left(\sqrt{\frac{1}{Runs} \cdot \sum_{j=1}^{j=Runs} (AoA2_{True}(j) - AoA2_{Estimated}(j))^2}\right) \qquad (46)$$

Where $AoA2_{True}$ represents the actual value of the angle of arrival of the received signal at the MS, calculated using equation 45. $AoA2_{Estimated}$ refers to the estimated value of the AoA of the received signal at the MS, determined using the MUSIC or MIN-NORM algorithms. Runs denote the number of iterations in the estimation process.

6 MUSIC Algorithm

6.1 Overview of MUSIC algorithm

The MUSIC algorithm is a spatial spectrum estimation algorithm that estimates the angle of arrival of a received signal using the orthogonality property between the signal subspace and the noise subspace. It employs eigenvalue decomposition (EVD) to separate the signal of interest from the noise by determining the array covariance matrix [49], [51], [61], [77]. With this technique, signal-based and noise-based subspaces can be effectively obtained. Then, the power spectrum function of the MUSIC algorithm is calculated, and the angle of arrival is estimated by searching for all arrival vectors that are orthogonal to the noise subspace. To do so, the algorithm constructs an arrival-angle-dependent power expression for the MUSIC pseudo-spectrum, which has infinite peaks when an arrival vector is orthogonal to the noise subspace. In practice, however, the angles at which the pseudo spectrum has finite peaks represent the desired arrival directions. Because the pseudo spectrum can have more peaks than there are sources, the algorithm requires that the number of sources, K, be specified as a parameter so that the K largest peaks are chosen.

6.2 Flow chart for MUSIC algorithm

Fig. 4 presents a flow chart for the MUSIC algorithm.

Data from the receiving antenna

Calculate the covariance matrix of the received signal

Perform eigenvalue and eigenvector decomposition

Calculate the noise subspace (E_N)

Calculate the MUSIC spectrum PMU(**angle**)

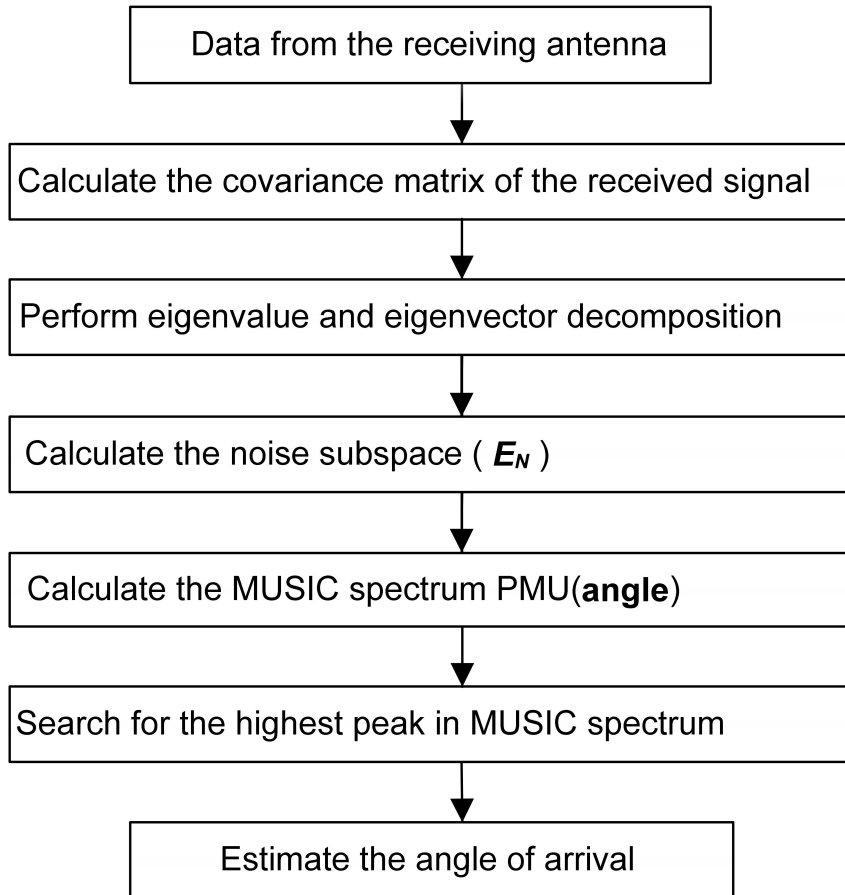Search for the highest peak in MUSIC spectrum

Estimate the angle of arrival

Figure 4: MUSIC implementation flow chart [1].

6.3 MUSIC implementation

MUSIC deals with the decomposition of the covariance matrix of the received signal at a mobile station into two orthogonal matrices: signal-subspace and noise-subspace. Estimation of direction is performed from one of these subspaces, assuming that noise in each channel is highly uncorrelated. The array covariance matrix has Nm eigenvalues $(\lambda_1, \lambda_2, \ldots, \lambda_{Nm})$ along with Nm associated eigenvectors E= $[e_1 \quad e_2 \quad e_{Nm}]$. If the eigenvalues are sorted from smallest to largest, we can divide the matrix E into two subspaces $[E_N \quad E_S]$. The first subspace E_N is called the noise subspace and is composed of Nm–K eigenvectors associated with the noise. Where K denotes the number of sources signals, in our scenario, K=1. The second subspace E_S is called the signal subspace and is composed of K eigenvectors associated with the source signals. The noise subspace is an $Nm \times (Nm - K)$ matrix, and the signal subspace is an $Nm \times K$ matrix. The noise subspace eigenvectors E_N are orthogonal to the array steering vectors $\mathbf{h}_{TOTAL}(\mathbf{angle})$ at the true angle of arrival. Because of this orthogonality condition $\mathbf{h}_{TOTAL}^H(\mathbf{angle})E_N E_N^H \mathbf{h}_{TOTAL}(\mathbf{angle}) = 0$ when **angle** equal true arrival angle. Placing this expression in the denominator creates sharp peaks at the true arrival angles. The MUSIC pseudo spectrum is now given as

$$PMU(\mathbf{angle}) = \frac{1}{\mathbf{h}_{TOTAL}^H(\mathbf{angle})E_N E_N^H . \mathbf{h}_{TOTAL}(\mathbf{angle})} \tag{47}$$

Where $(.)^H$ denotes the Hermitian operator.
MUSIC calculates the PMU(**angle**) at each **angle** $\in$ [0,180] of all the samples, then calculates the average PMU(**angle**) at each angle. After that, it searches for the maximum average PMU(**angle**); the **angle** with the highest average PMU(**angle**) represents the intended angle of arrival.

6.3.1 MUSIC spectrum PMU(angle)

To further explain how to calculate the MUSIC spectrum, follow these steps.

Step 1: Find the noise subspace E_N.

Step 2: Calculate the PMU(**angle**) at each **angle** from 0 to 180 for all samples.

$$PMU(\mathbf{angle}) = \frac{1}{\mathbf{h}_{TOTAL}^H(\mathbf{angle})E_N E_N^H \mathbf{h}_{TOTAL}(\mathbf{angle})} \tag{48}$$

where,
$\mathbf{h}_{TOTAL}(\mathbf{angle})$ for any sample = $\mathbf{G}_T(\mathbf{angle})\Phi_T(\mathbf{angle})\mathbf{h}_T$

23

$$\mathbf{G}_T(\mathbf{angle}) = \left(\frac{\lambda}{4\pi d_2^{\eta/2}}\right) \mathbf{z}_T(\mathbf{angle})\mathbf{g}_T(\mathbf{angle}),$$

$$\mathbf{z}_T(\mathbf{angle}) = \begin{bmatrix} 1 \\ e^{-j2\pi\frac{d}{\lambda}cos(\mathbf{angle})} \\ e^{-j2\pi(Nm-1)\frac{d}{\lambda}cos(\mathbf{angle})} \end{bmatrix} \quad \begin{bmatrix} \rho_1 & \rho_2 & \rho_T \end{bmatrix}$$

$$\mathbf{g}_T(\mathbf{angle}) = \begin{bmatrix} \beta_1 \\ \beta_2 \\ \beta_T \end{bmatrix} \quad \begin{bmatrix} 1 & e^{-j2\pi\frac{d}{\lambda}cos(-180+\mathbf{angle})} & e^{-j2\pi(Nr-1)\frac{d}{\lambda}cos(-180+\mathbf{angle})} \end{bmatrix}$$

$$\Phi_T(\mathbf{angle}) = [diag(\mathbf{q}_1(\mathbf{angle})) \quad diag(\mathbf{q}_2(\mathbf{angle})) \quad diag(\mathbf{q}_T(\mathbf{angle}))] \tag{49}$$

$$\mathbf{q}_1(\mathbf{angle}) = \begin{bmatrix} e^{-j(b_1+F_1)} \\ e^{-j(b_1-\frac{2\pi dcos(-180+\mathbf{angle})}{\lambda}+F_1-\frac{2\pi dcos(AoA1)}{\lambda})} \\ e^{-j(b_1-\frac{2\pi(Nr-1)dcos(-180+\mathbf{angle})}{\lambda}+F_1-\frac{2\pi(Nr-1)dcos(AoA1)}{\lambda})} \end{bmatrix} \tag{50}$$

$$\mathbf{h}_T = \left(\frac{\lambda}{4\pi d_1^{\eta/2}}\right) \begin{bmatrix} 1 \\ e^{-j2\pi\frac{d}{\lambda}cos(AoA1)} \\ e^{-j2\pi(Nr-1)\frac{d}{\lambda}cos(AoA1)} \end{bmatrix} \quad \begin{bmatrix} \alpha_1 & \alpha_2 & \alpha_T \end{bmatrix} \tag{51}$$

Step 3: Calculate the average PMU (**angle**) at each angle.

Step 4: Search for the maximum average PMU(**angle**).

Step 5: Decide the angle with the highest average PMU(**angle**) representing the intended arrival angle.

6.3.2 Noise subspace

To calculate the noise subspace $\mathbf{E}_N$, follow these steps:-
Step 1: Find the Covariance matrix of the received signal $cov(\mathbf{y}_T) \in \mathbb{C}^{Nm\times Nm}$.

$$cov(\mathbf{y}_T) = \frac{\mathbf{y}_T\mathbf{y}_T^H}{T} \tag{52}$$

Step 2: Decompose the eigenvalues and arrange them in ascending order, which $\lambda = \begin{bmatrix} \lambda_1 & 0 & 0 \\ 0 & \lambda_2 & 0 \\ 0 & 0 & \lambda_{Nm} \end{bmatrix}$

Step 3: Find eigenvectors associated with $Nm-K$ smallest eigenvalue.

Step 4: The $(Nm \quad X \quad Nm$ -$K)$ eigenvectors denote the noise subspace E_N.

6.3.3 Generate data

To generate data, follow these steps.

Step 1: Specify the location of the BS and the RIS.

Step 2: Assign a random location for the MS.

Step 3: Generate a T-sample.

Step 4: Send sample 1 (T_1).

Step 5: Apply a fading channel between the BS and the RIS using equations (14), and (43).

Step 6: Adjust the phase shift for each element at the RIS to maximize the received signal power at the MS using Equations (28), (43) and (44).

Step 7: Apply a fading channel between the RIS and the MS using equations (15), (19), (23), (44), and (45).

Step 8: Send other samples to the MS.

Step 9: Repeat Steps 6-7-8 using equation (32),(33),(34),(35), and (36).

Step 10: Calculate the total received signal from the T-sample at MS using equation (31).

7 MIN-NORM Algorithm

7.1 Overview of MIN-NORM algorithm

Kumaresan and Tufts proposed the MIN-NORM algorithm [12] for frequency analysis and antenna processing. It is another method based on eigendecomposition; instead of forming an eigenspectrum that utilizes all of the noise eigenvectors as in the MUSIC and eigenvector algorithms, this method consists of searching for $\mathbf{a}$ vector with the Minimum Norm within the noise subspace to determine the position of the peaks in the pseudo-spectrum.

To calculate this vector, three constraints must be satisfied [13]:
1) The vector $\mathbf{a}$ must lie within the noise subspace E_N, then it is orthogonal to the projection on the signal subspace, $E_s^H.\mathbf{a} = 0$.
2) The vector $\mathbf{a}$ has a Minimum Norm.
3) The first element of $\mathbf{a}$ is unity.

The third constraint can be expressed as follows:

$$\mathbf{a}^H.\mathbf{u}_1 = 1 \tag{53}$$

where $\mathbf{u}_1 = \begin{bmatrix} 1 \\ 0 \\ 0 \end{bmatrix} \qquad \mathbf{u}_1 \in \subset^{Nm \times 1}$

Therefore, the Minimum Norm solution as mentioned in [78] is:

$$\mathbf{a} = \frac{E_N.E_N^H.\mathbf{u}_1}{\mathbf{u}_1^H.E_N.E_N^H.\mathbf{u}_1} \tag{54}$$

The MIN-NORM pseudo spectrum [78] is given as

$$P_{MIN-NORM}(\mathbf{angle}) = \frac{1}{|\mathbf{h}_{TOTAL}^H(\mathbf{angle}).\mathbf{a}|^2}$$

$$\tag{55}$$

$$= \frac{1}{\mathbf{h}_{TOTAL}^H(\mathbf{angle}).\mathbf{a}.\mathbf{a}^H.\mathbf{h}_{TOTAL}(\mathbf{angle})}$$

7.2   Flow chart for MIN-NORM algorithm

Fig. 5 presents a flow chart for the MIN-NORM algorithm.

```
┌─────────────────────────────────────────┐
│      Data from the receiving antenna      │
└─────────────────────────────────────────┘
                    │
                    ▼
┌─────────────────────────────────────────┐
│ Calculate the covariance matrix of the received signal │
└─────────────────────────────────────────┘
                    │
                    ▼
┌─────────────────────────────────────────┐
│  Perform eigenvalue and eigenvector decomposition  │
└─────────────────────────────────────────┘
                    │
                    ▼
┌─────────────────────────────────────────┐
│    Calculate the noise subspace ( EN )    │
└─────────────────────────────────────────┘
                    │
                    ▼
┌─────────────────────────────────────────┐
│    Calculate the Minimum Norm solution (a) │
│                                           │
│         a = (E_N.E_N^H.u_1)/(u_1^H.E_N.E_N^H.u_1) │
└─────────────────────────────────────────┘
                    │
                    ▼
┌─────────────────────────────────────────┐
│   Calculate the MIN-NORM spectrum (angle) │
│                                           │
│  P_MIN-NORM(angle) = 1/|h_TOTAL^H(angle).a|^2 │
└─────────────────────────────────────────┘
                    │
                    ▼
┌─────────────────────────────────────────┐
│  Search for the highest peak in MIN- NORM spectrum │
└─────────────────────────────────────────┘
                    │
                    ▼
┌─────────────────────────────────────────┐
│        Estimate the angle of arrival       │
└─────────────────────────────────────────┘
```

Calculate the Minimum Norm solution (a)

$$\mathbf{a} = \frac{E_N.E_N^H.\mathbf{u}_1}{\mathbf{u}_1^H.E_N.E_N^H.\mathbf{u}_1}$$

Calculate the MIN-NORM spectrum (angle)

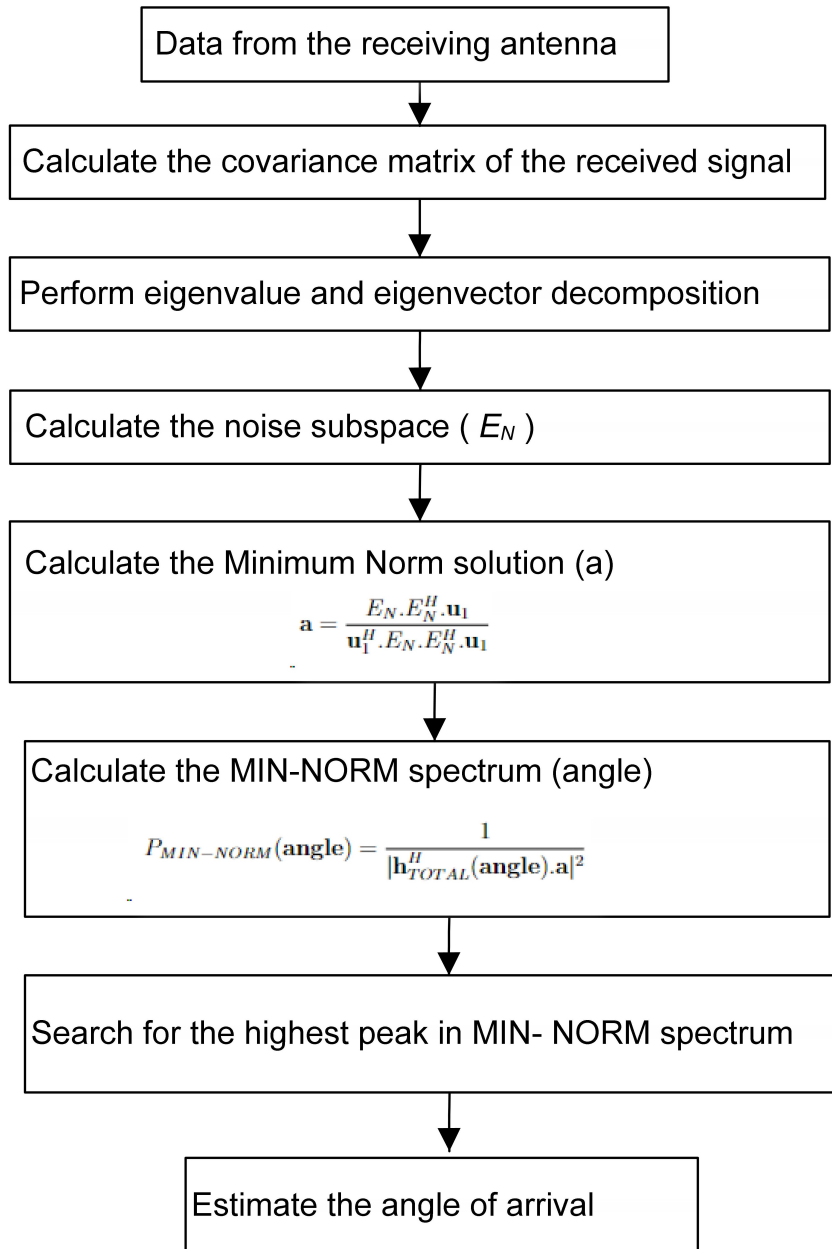$$P_{MIN-NORM}(\mathbf{angle}) = \frac{1}{|\mathbf{h}_{TOTAL}^H(\mathbf{angle}).\mathbf{a}|^2}$$

Figure 5:   MIN-NORM implementation flow chart.

8 Numerical Simulation Results

We used MATLAB software to analyze the performance of the MUSIC algorithm and the MIN-NORM algorithm in estimating the angle of arrival of the received signal at the MS.

8.1 Simulation setup

The main simulation parameters are presented in Table 2.

Table 2: Simulation parameters.

Parameters	Values
System Bandwidth (BW)	1 MHz
Power of AWGN (No)	-114 dBm
Transmitted Power (P_t)	1 W
Carrier Frequency (f_c)	30 GHz
True value for AoA2	115
Number of Sources Signal (K)	1
Path loss exponent at all links (η)	2
Inter-Element Spacing in the Array (d)	$\lambda/2 = 0.005$
Wavelength for the Carrier Frequency (λ)	0.01m
Number of Array Elements at RIS (Nr)	200
Number of Array Elements at MS (Nm)	20
Number of Snapshots or Samples (T)	500
The location of the base station (b_x, b_y)	(0,0)
The location of the RIS relative to the origin (r_x, r_y)	(10,15)
The location of the mobile station relative to the origin(m_x, m_y)	(17,0)

8.2 Results

In this part, we present the results of the angle of arrival estimation obtained using the MUSIC algorithm. Furthermore, we employed the MIN-NORM algorithm to validate the performance and effectiveness of the MUSIC algorithm in the angle of arrival estimation. The estimation efficiency can be optimized by considering various parameters, such as:

1. Increasing the number of array elements at the RIS.

Fig. 6 illustrates the impact of the number of elements at RIS on the MUSIC spectrum, while Fig. 7 demonstrates the effect of the number of elements at RIS on the MIN-NORM spectrum, with all other simulation parameters held constant.
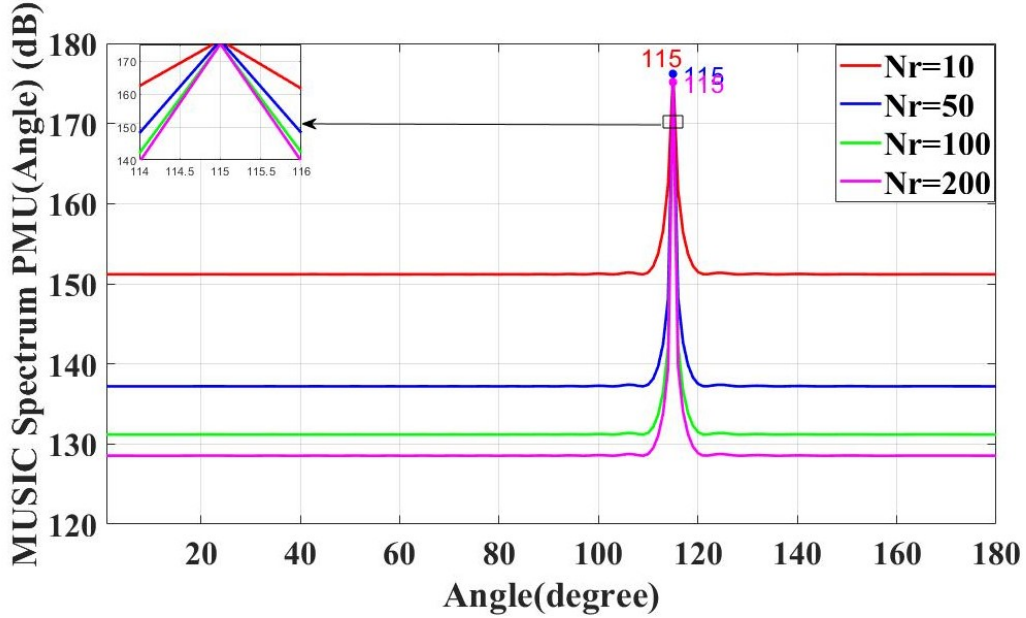

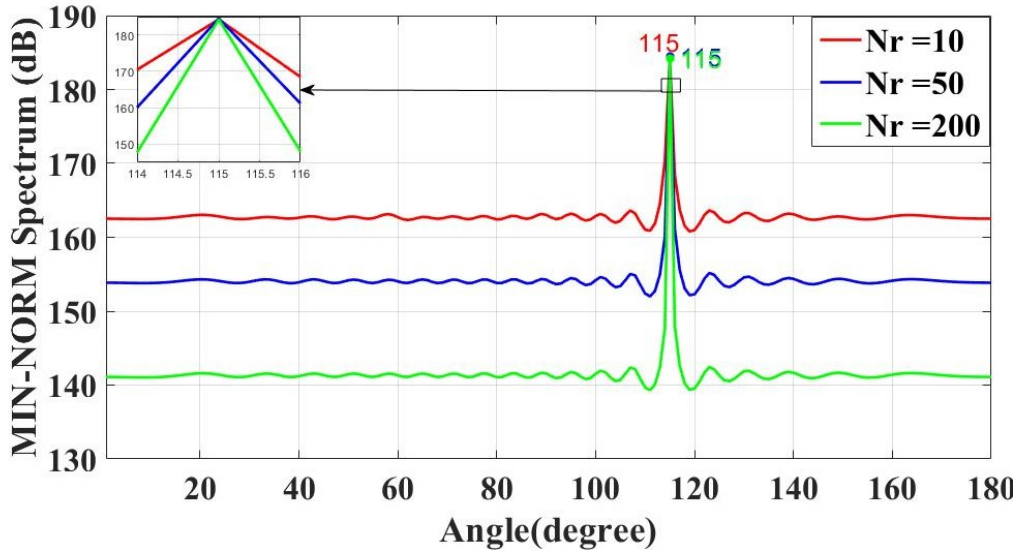Figure 6: MUSIC algorithm performance for different array elements at RIS.

Figure 7: MIN-NORM algorithm performance for different array elements at RIS.

The simulation results in Fig. 6 and Fig. 7 demonstrate that the performance of the MUSIC algorithm and the MIN-NORM algorithm improves with an increased number of elements at the RIS. Sharper peaks and narrower beamwidth in the spectra indicate this

29

improvement. These enhancements signify a clearer signal direction, higher accuracy in estimating the angle of arrival, and improved directivity and beamforming gain.

Furthermore, we will examine the impact of changing the number of RIS elements on the received signal strength. We calculated the power received (Pr) at the mobile station using equation (39) and evaluated the SNR using equation (41). The results were subsequently included in Table 3.

Table 3: Received signal power and SNR at the mobile station for different array elements at RIS (Nm = 20, T = 500, $\eta = 2, d = \lambda/2, Ps = 1watt$).

Nr	Pr (dBm)	SNR (dB)
10	-113.81	0.194
50	-99.83	14.174
100	-93.81	20.194
200	-87.90	26.105

The results presented in Table 3 indicate that as the number of elements at the RIS increases, both the received signal power and SNR at the mobile station also increase. This improvement in signal strength signifies an enhancement in link quality. Hence, a larger number of RIS elements is crucial for establishing a reliable connection through the reflected path.

When comparing the results in Fig. 6 with Table. 3, it is evident that an increased number of elements at the RIS results in higher received signal power at the mobile station, an increased SNR, a sharper MUSIC spectrum, and a narrower beamwidth in the MUSIC spectrum. These outcomes contribute to enhanced directivity, resulting in improved accuracy in estimating the angle of arrival.

Fig. 8 shows the RMSE results of the angle of arrival estimation concerning the number of RIS elements, keeping all other simulation parameters constant. The Monte Carlo estimations were performed over 100 simulations. With the results presented, it is possible to verify that the MUSIC technique has the best performance when the number of RIS elements is 6 elements or more, but the MIN-NORM technique performs best when the number of RIS elements is 12 elements or more.
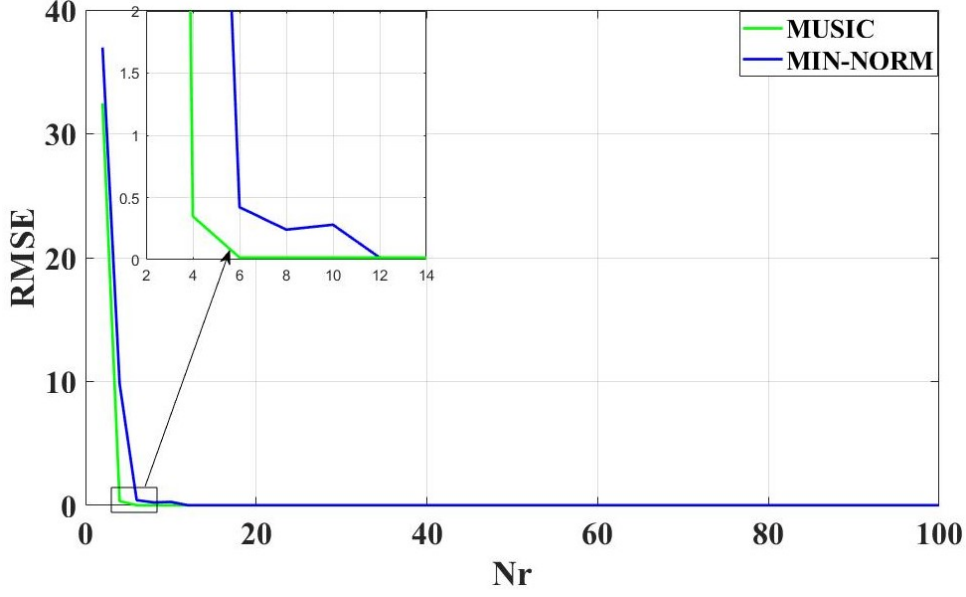
Figure 8: RMSE versus number of array elements at RIS($Nm = 20$, T $= 500$, $\eta = 2, d = \lambda/2, Ps = 1Watt$).

Fig. 9 presents the angle of arrival estimation results by MUSIC and MIN-NORM when the number of array elements at RIS $= 50$
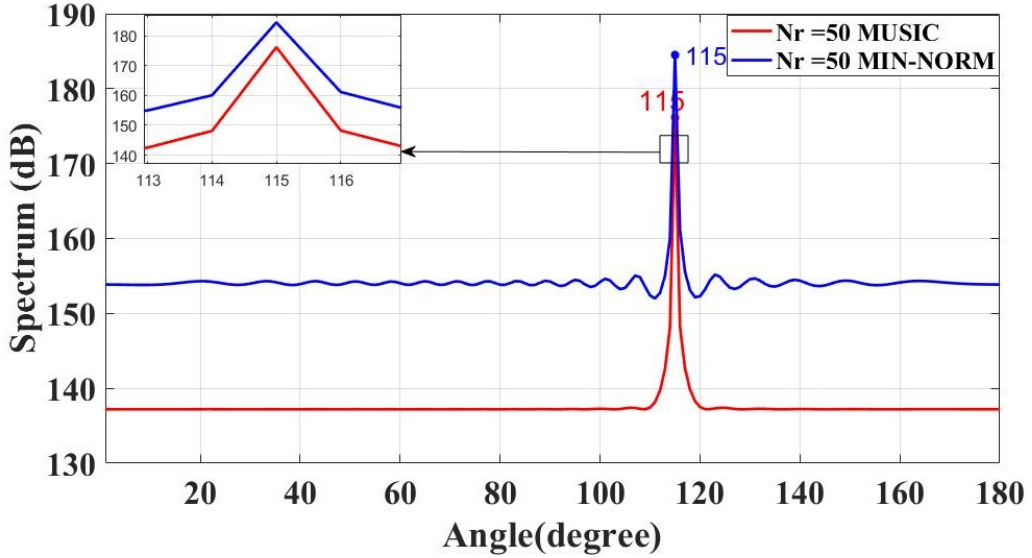

Figure 9: The performance of the MUSIC and MIN-NORM algorithms when Nr $= 50$, Nm=20, T $= 500$, d= $\lambda/2, \eta = 2, Ps = 1watt$.

The results in Fig. 9 show that both algorithms provide high accuracy in estimating the angle of arrival of the received signal. However, the beam width in the MUSIC algorithm is narrower than that of MIN-NORM. As a result, the MUSIC algorithm increases directivity and beamforming gain. Additionally, the MUSIC algorithm does not produce any additional small peaks like the MIN-NORM algorithm, which increases the efficiency of the MUSIC algorithm.

31

2. Increasing the number of snapshots.

Fig. 10 depicts the impact of the number of snapshots on the MUSIC spectrum, while Fig. 11 demonstrates the effect of the number of snapshots on the MIN-NORM spectrum, with all other simulation parameters being kept constant.
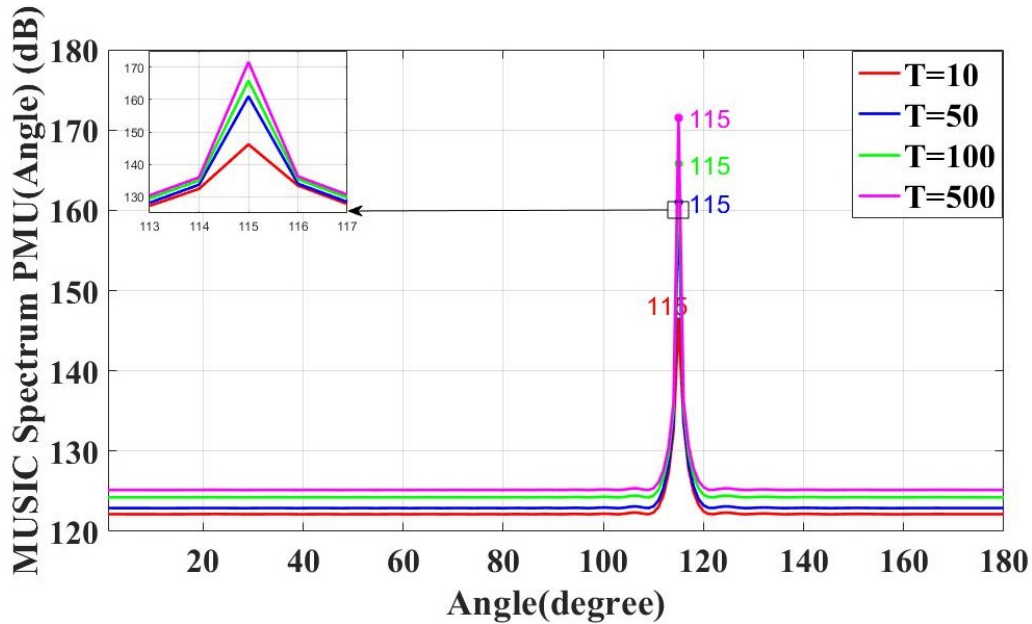

Figure 10: MUSIC algorithm performance for a different number of snapshots.
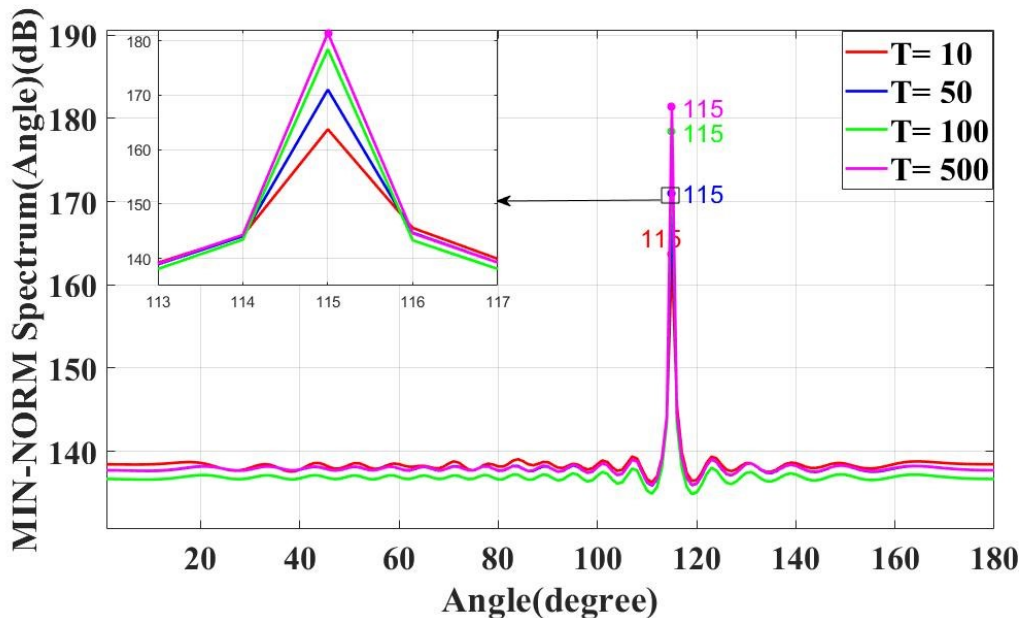

Figure 11: MIN-NORM algorithm performance for a different number of snapshots.

The results depicted in Fig. 10 and Fig. 11 indicate that an increasing number of snapshots result in sharper peaks in the MUSIC spectrum and MIN-NORM. This leads to

more precise direction-of-arrival estimation and improved directivity, thereby enhancing the efficiency of the estimation algorithms. However, the inclusion of more samples also leads to increased data processing and computation, resulting in slower speed. Consequently, it is crucial to select an appropriate number of snapshots that meets the accuracy requirements while minimizing resource consumption and maximizing speed.

Table. 4 illustrates the received power and SNR, calculated using equations (39) and (41) respectively while varying the number of snapshots. We will analyze the impact of the number of snapshots and SNR value on the estimated angle of arrival.

Table 4: Received signal power and SNR at the mobile station for different numbers of snapshots (Nm = 20, Nr = 200, d = $\lambda/2, \eta = 2, Ps = 1watt$).

T	Pr (dBm)	SNR (dB)
10	-88.94	25.06
50	-88.44	25.56
100	-88.7	25.3
500	-87.79	26.2

When comparing the results in Fig. 10 with those in Table. 4, we observe that if the SNR is good, only a few snapshots are sufficient to estimate the angle of arrival accurately; in this case, 50 or 100 snapshots are enough.

Furthermore, we studied the effect of increasing the number of snapshots on the MUSIC spectrum in Shadowed urban cellular radio by increasing the path loss exponent to 3.5 while keeping all other simulation parameters constant. The results of the simulation are presented in Fig. 12.
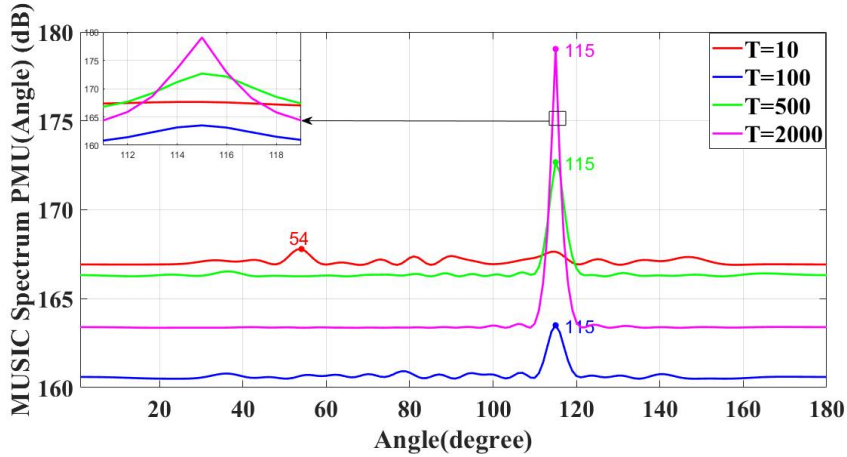
Figure 12: MUSIC algorithm performance for a different number of snapshots($\eta = 3.5, Nm = 20, Nr = 200, Ps = 1watt, d = \lambda/2$).

The results of Fig. 12 indicate that in Shadowed urban cellular radio, MUSIC works correctly with fewer errors and sharper peaks when higher numbers of snapshots are used.

Table 5: Received signal power and SNR at the mobile station for different numbers of snapshots ($\eta = 3.5, Nm = 20, Nr = 200, Ps = 1watt, d = \lambda/2$).

T	Pr (dBm)	SNR (dB)
10	-125.86	-11.87
100	-125.96	-11.96
500	-125.8	-11.36
2000	-124	-10

When comparing the results in Fig. 12 with those in Table. 5, We observe that the estimation task becomes more difficult with lower SNR values and fewer snapshots. Therefore, if the SNR is very low, MUSIC needs more snapshots to increase the efficiency of the estimation algorithm. The more snapshots, the narrower the peaks. In this case, it is observed that 2000 snapshots are needed in order to accurately estimate the angle of arrival.

Fig. 13 presents the RMSE results for the angle of arrival estimation based on the number of snapshots while keeping all other simulation parameters constant. The Monte Carlo estimations were conducted across 100 simulations. The findings demonstrate that both the MUSIC and MIN-NORM algorithms exhibit superior performance when the number of snapshots is 6 or greater.

Fig. 14 displays the performance of the angle of arrival estimation algorithms when the
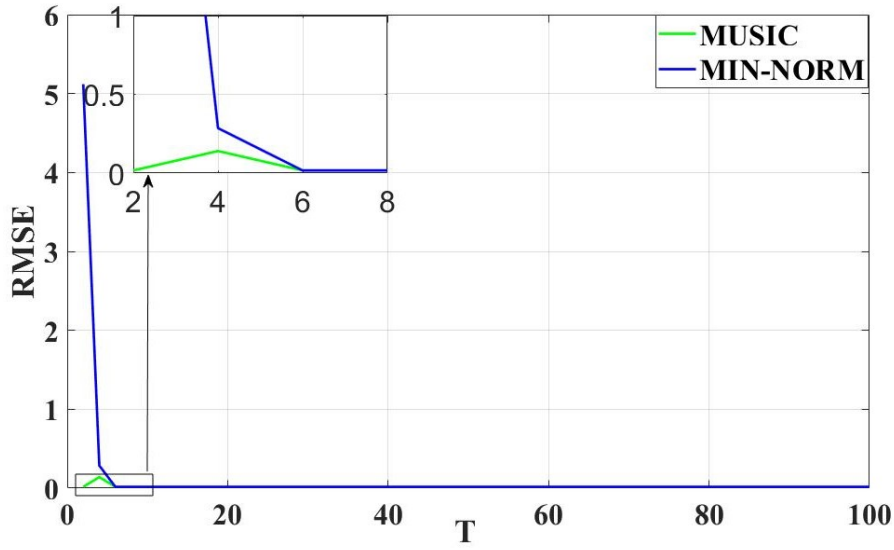
34

Figure 13: RMSE Versus number of snapshots (Nm = 20, Nr = 200, $\eta = 2, Ps = 1watt$).

number of snapshots is set to 100. The results demonstrate the high accuracy of both the MIN-NORM and MUSIC algorithms in estimating the arrival angle of the received signal. These findings confirm the effectiveness of the algorithms in accurately estimating the angle of arrival. Specifically, the MUSIC technique outperforms the MIN-NORM technique with a narrower beam width and does not exhibit any additional small peaks.
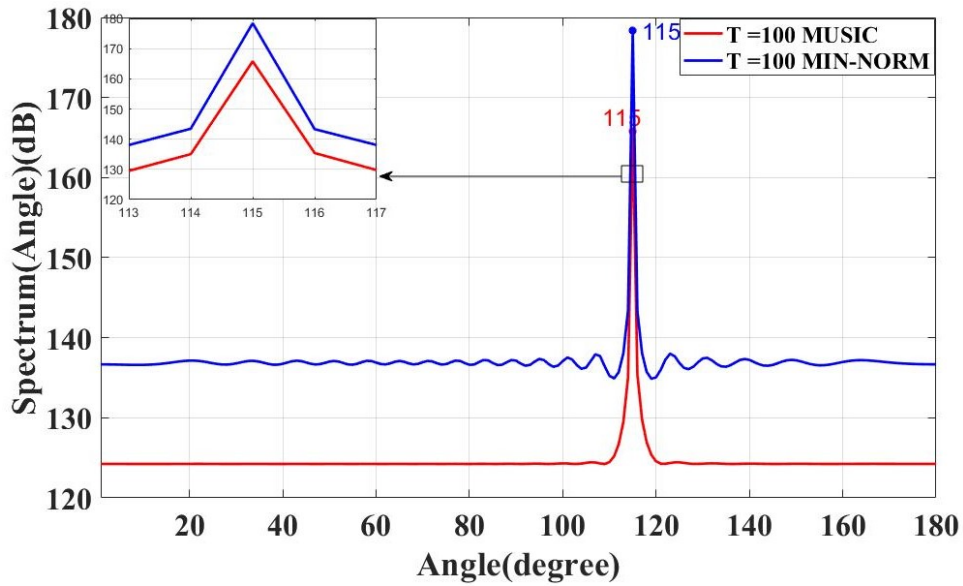

Figure 14: The performance of the MUSIC and MIN-NORM algorithms when (T = 100, Nm = 20, Nr = 200, $\eta = 2, Ps = 1watt, d = \lambda/2$).

3. Increasing the number of array elements at the mobile station.

Fig. 15 depicts the influence of the number of array elements at the mobile station on the MUSIC spectrum, while Fig. 16 presents the effect on the MIN-NORM spectrum, keeping all other simulation parameters constant.
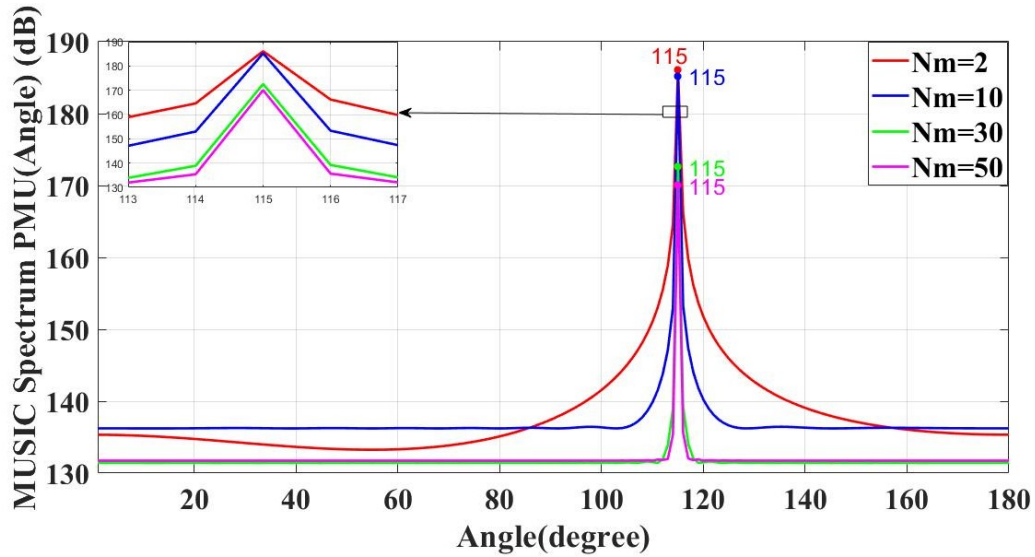

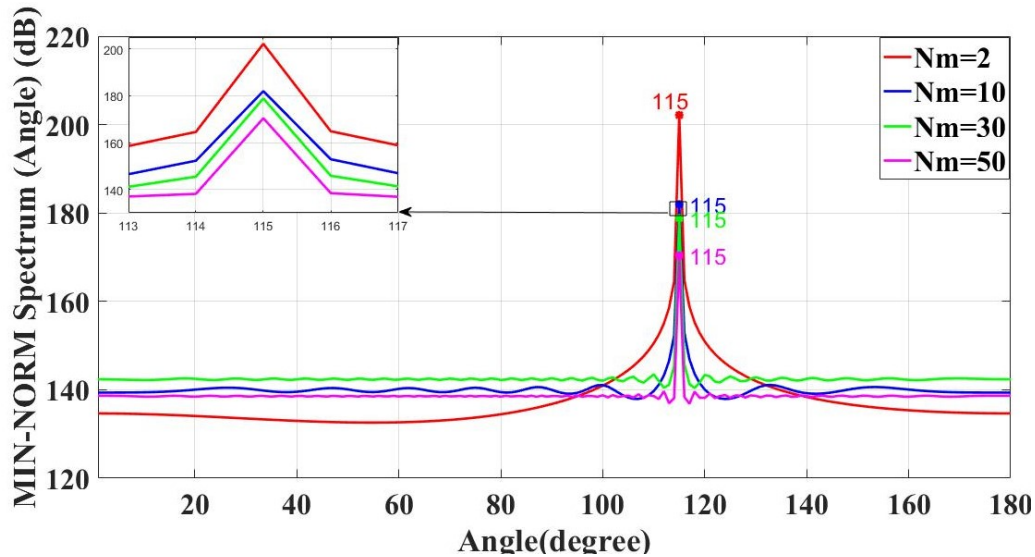Figure 15: MUSIC algorithm performance for different array elements at MS.

Figure 16: MIN-NORM algorithm performance for different array elements at MS.

The results presented in Fig. 15 and Fig. 16 demonstrate that increasing the number of array elements at the mobile station leads to a narrower beamwidth in both the MUSIC spectrum and the MIN-NORM spectrum. This enhancement improves the resolution of the direction-of-arrival spectrum, resulting in a needle-like peak and increased directivity

36

of the antenna array. Consequently, the beamforming gain is increased, enabling the antenna beam to effectively focus on the intended user. Additionally, increasing the number of array elements at the mobile station causes the disappearance of additional small peaks in the MIN-NORM spectrum. This improvement contributes to the increased efficiency of the MIN-NORM algorithm.

Fig. 17 shows the RMSE results of the angle of arrival estimation with respect to the number of array elements at the mobile station, keeping all other simulation parameters constant. The Monte Carlo estimations were performed over 100 simulations. Based on the presented results, both algorithms yield an RMSE of 0.017 for any value of the number of array elements at the MS.
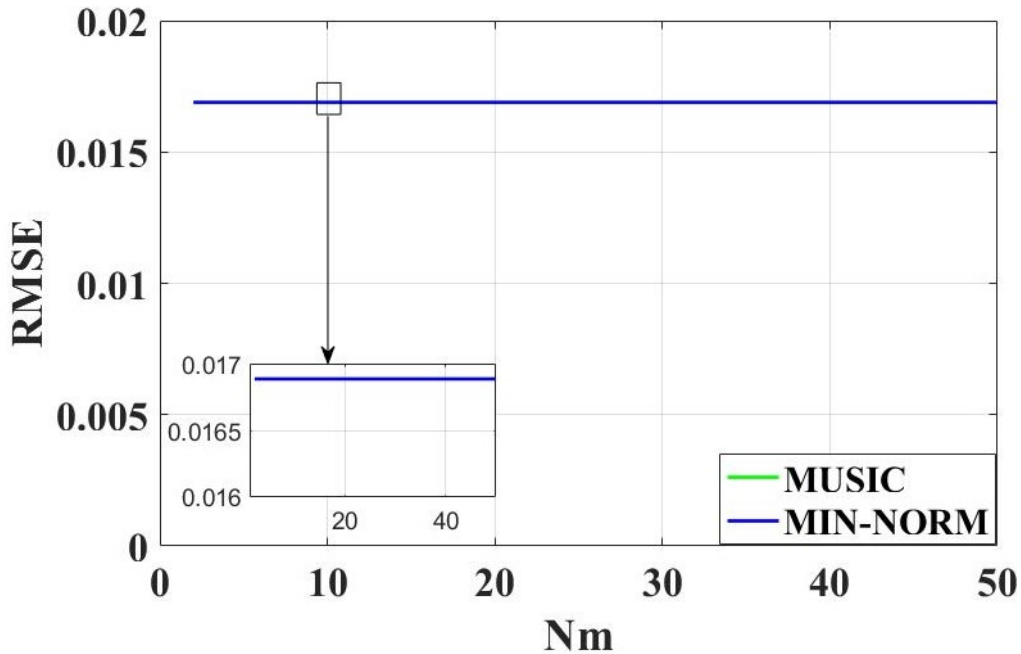

Figure 17: RMSE Versus Number of array elements at the mobile station (T = 500, Nr = 200, $\eta = 2, Ps = 1watt, d = \lambda/2$).

Fig. 18 displays the angle of arrival estimation results obtained by the MUSIC and MIN-NORM algorithms when the number of array elements at MS = 70. The results indicate that both algorithms demonstrate high accuracy in estimating the angle of arrival of the received signal. Moreover, the MUSIC algorithm outperforms the MIN-NORM algorithm by achieving a narrower beam width.

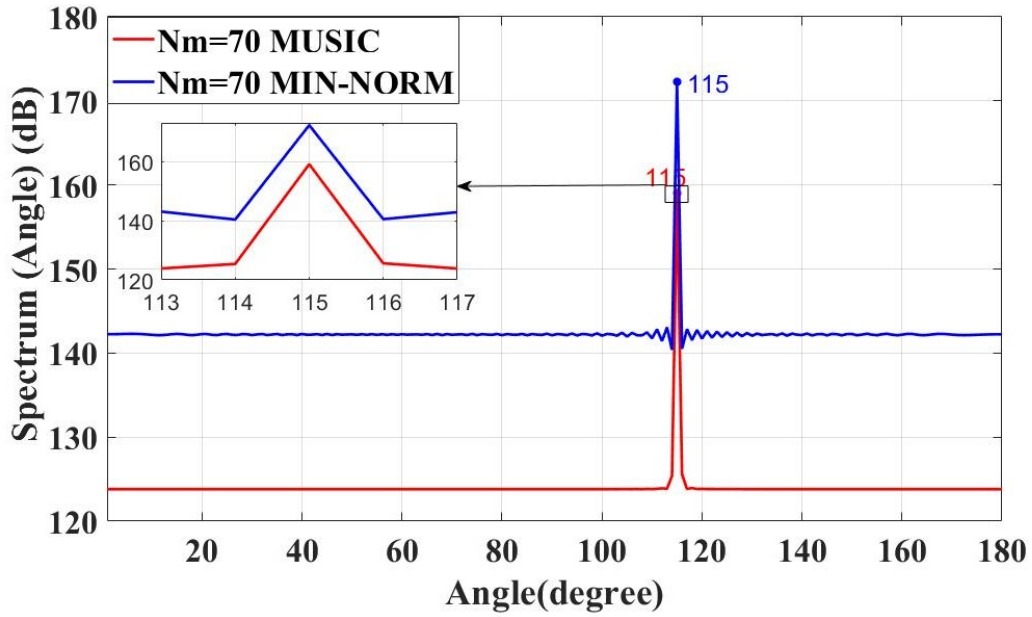Figure 18: The performance of the MUSIC and MIN-NORM algorithms (when Nm = 70, T = 500, Nr = 200, $\eta = 2, Ps = 1watt, d = \lambda/2$).

4. Increasing SNR.

The influence of the SNR on the MUSIC spectrum is illustrated in Fig. 19, while the effect of SNR on the MIN-NORM spectrum is depicted in Fig. 20. All other simulation parameters remain constant.
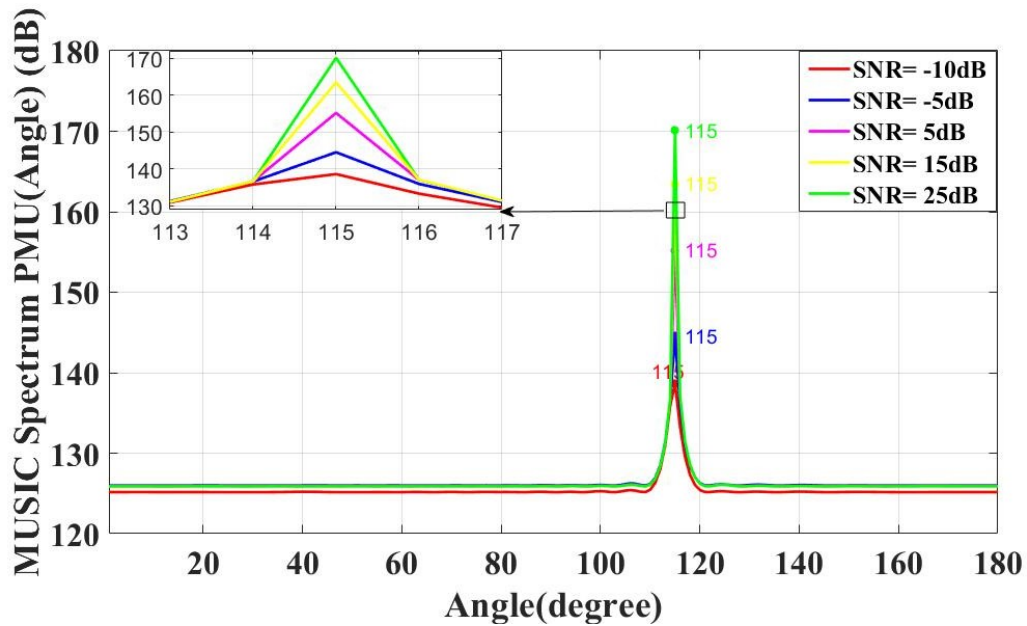

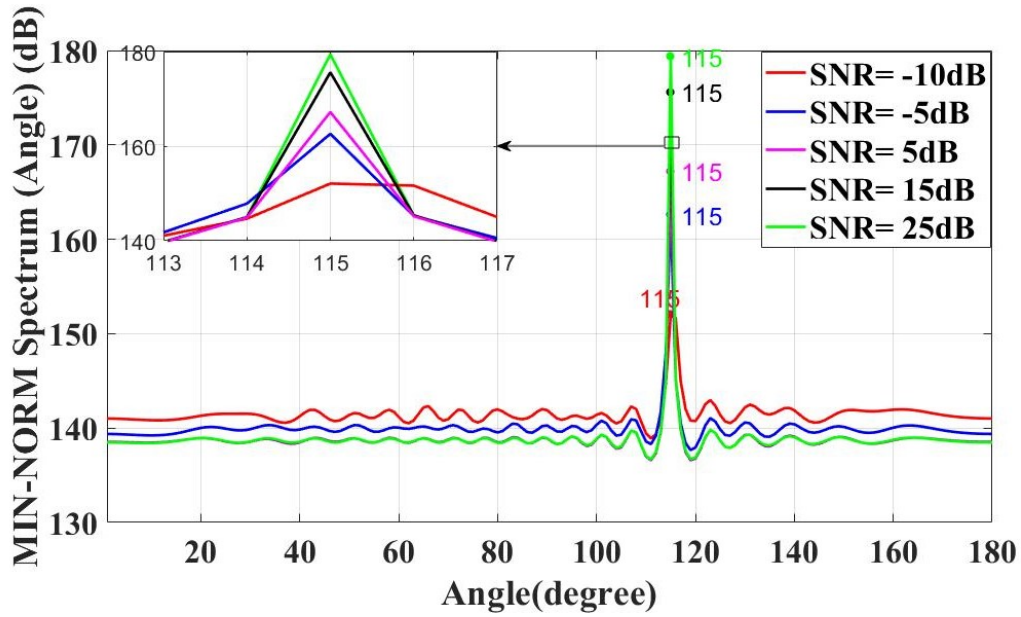Figure 19: MUSIC algorithm performance for different SNRs.

Figure 20: MIN-NORM algorithm performance for different SNRs

When the SNR increases, indicating a less noisy environment and better link quality, it has a direct and positive impact on the performance of both the MUSIC and MIN-NORM algorithms, as demonstrated in Fig. 19 and Fig. 20. The results indicate that as the SNR increases, the MUSIC spectrum and MIN-NORM spectrum exhibit sharper peaks, leading to reduced errors, improved accuracy in angle detection, and a clearer indication of the signal direction.

In Fig. 21, the performance of the angle of arrival estimation algorithms is showcased for a scenario where SNR 25 dB. The results show the accuracy of both the MIN-NORM and MUSIC algorithms in estimating the arrival angle of the received signal. The MUSIC and MIN-NORM algorithms exhibit clear and sharp peaks. Notably, the MUSIC technique outperforms the MIN-NORM technique with a narrower beam width and the absence of any additional small peaks.
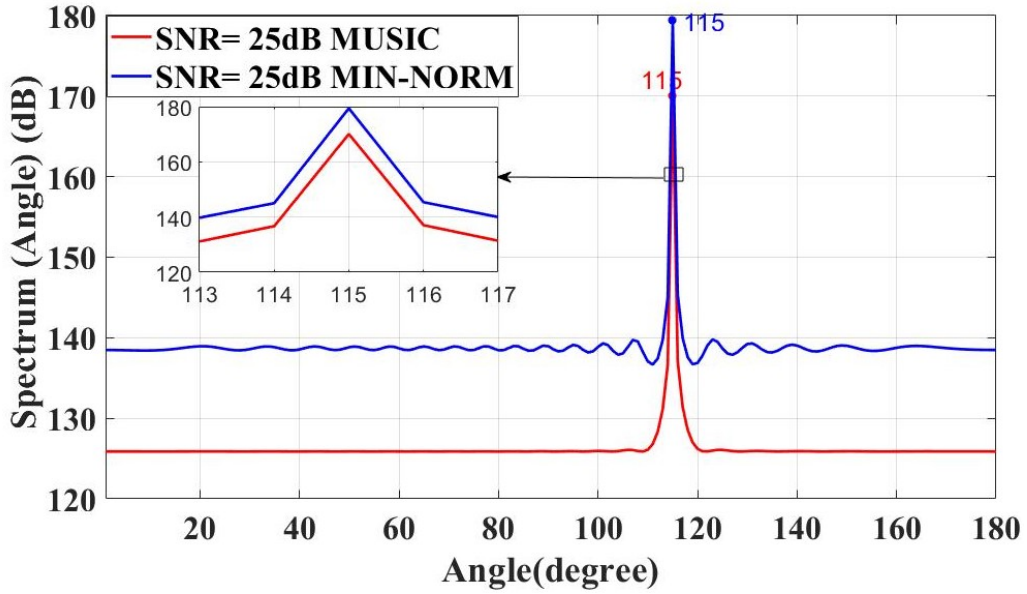
Figure 21: The performance of the MUSIC and MIN-NORM algorithms (when SNR =25 dB, Nm = 20, T = 500, Nr = 200, $\eta = 2, d = \lambda/2$)

5. The Spacing between array elements.

Inter-element spacing is an essential factor in designing an antenna array; the effect of inter-element spacing on the MUSIC spectrum is shown in Fig. 22 and Fig. 24, and the effect of inter-element spacing on the MIN-NORM spectrum is shown in Fig. 23 and Fig. 25. All other simulation parameters are the same.

Figure 22: Performance of the MUSIC algorithm for different array spacing ranging from 0.1λ to 0.6λ.

Figure 23: Performance of the MIN-NORM algorithm for different array spacing ranging from 0.1λ to 0.6λ.

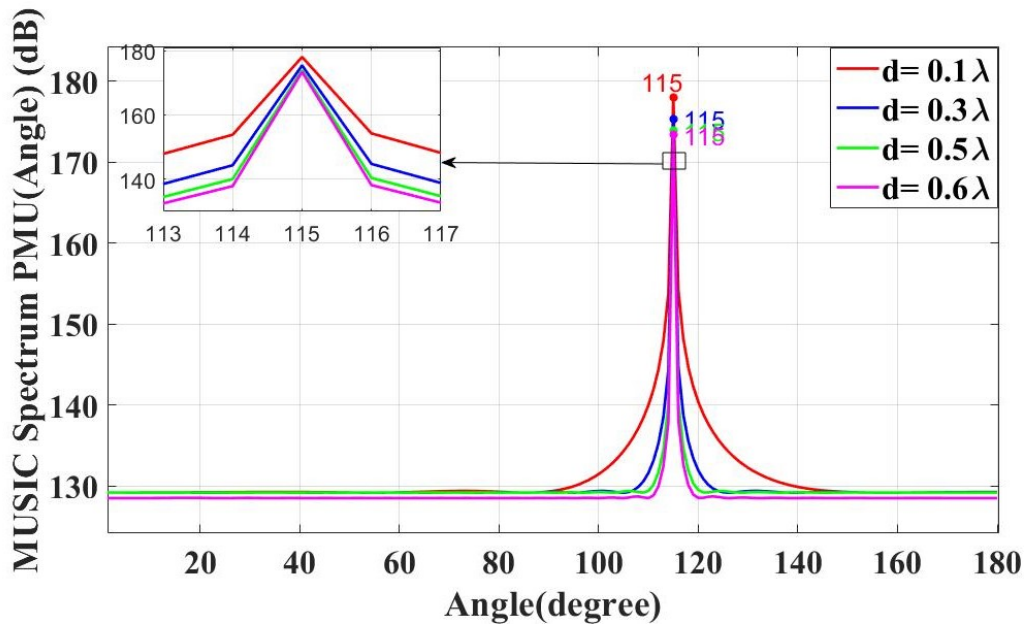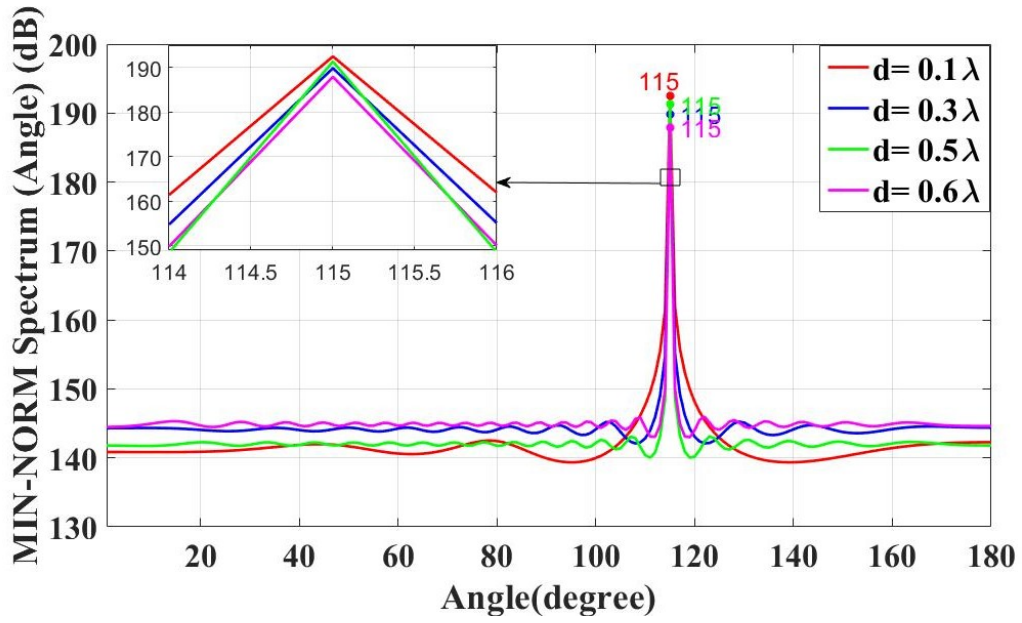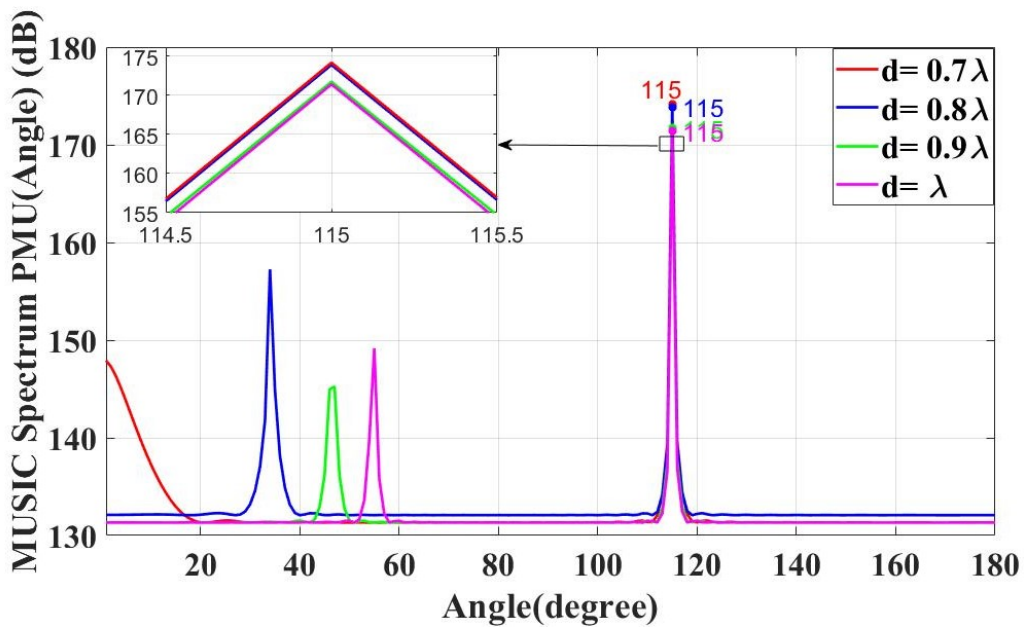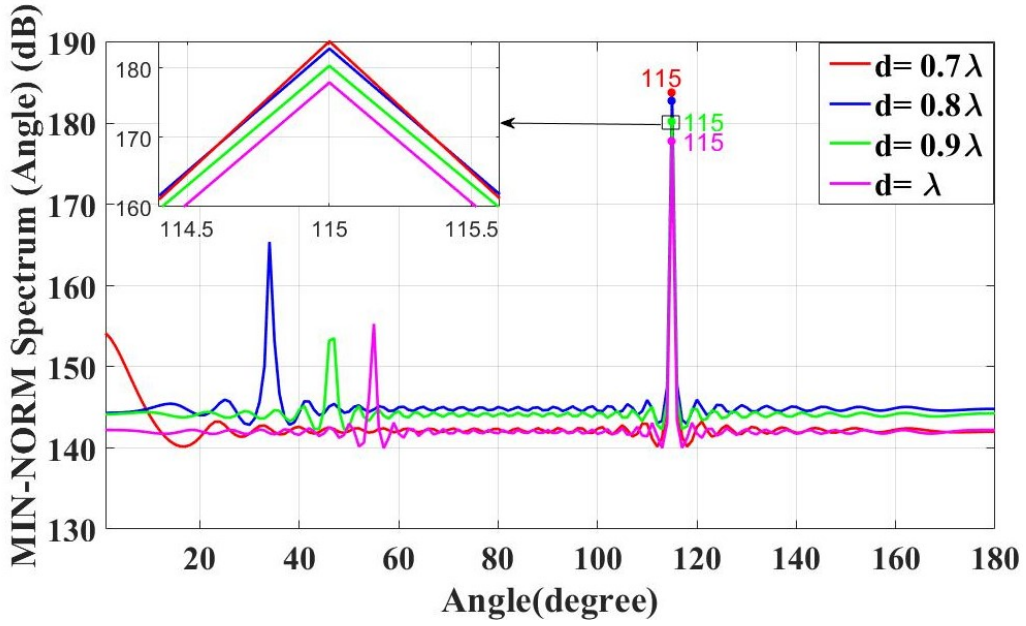Figure 24: Performance of the MUSIC algorithm for different array spacing ranging from 0.7λ to λ.

Figure 25: Performance of the MIN-NORM algorithm for different array spacing ranging from 0.7λ to λ.

The simulated results shown in Fig. 22 and Fig. 23 indicate that the spacing affects the beam width of the MUSIC spectrum and the MIN-NORM spectrum. Consequently, as the inter-element spacings increase from 0.1λ to 0.6λ, the directivity of the array antenna also increases. The simulated results shown in Fig. 24 and Fig. 25 indicate that increasing the spacing beyond 0.7λ to 1.0λ also improves the directivity but introduces other directions known as grating lobes. These false peaks may result in the wrong estimation of the angle of arrival when the peak of the grating lobe is higher than the peak at the actual angle of arrival. If the elements are spaced too closely together (with a smaller d value), the coupling effect will be greater. On the other hand, if the elements are spaced too far apart, grating lobes will appear. Consequently, the elements must be sufficiently spaced apart to avoid mutual coupling, while still being close enough together to avoid grating lobes.

As per the author [79], it has been mentioned that the expression representing the maximum spacing between elements in a linear array with a rectangular lattice, to ensure avoidance of grating lobes at a scan angle of θ_0, can be expressed as:

$$dmax = \frac{\lambda}{(1 + |cos\theta_0|)} \tag{56}$$

By utilizing equation (56) within our system, we obtain the inter-element spacing in a

42

ULA at the mobile station where grating lobes become apparent.

$$dmax = \frac{\lambda}{(1 + |cos\theta_0|)} = \frac{\lambda}{(1 + |cos(115)|)} = 0.7\lambda \tag{57}$$

To validate the suitability of this law for calculating the distance at which grating lobes start to appear, let's present some additional examples:

In the context of a mobile station, when the location changes, the angle of arrival of the signal at the mobile will also change. This change in angle can be considered as the equivalent scan angle for which we need to calculate the inter-element distance of the antenna array at which grating lobes start to appear. By applying the law proposed by the author [79], we can determine the suitable distance between the elements to ensure grating lobes avoidance for the given angle of arrival.

Fig. 26 depicts the inter-element spacing in which grating lobes become apparent at an angle of arrival 135.
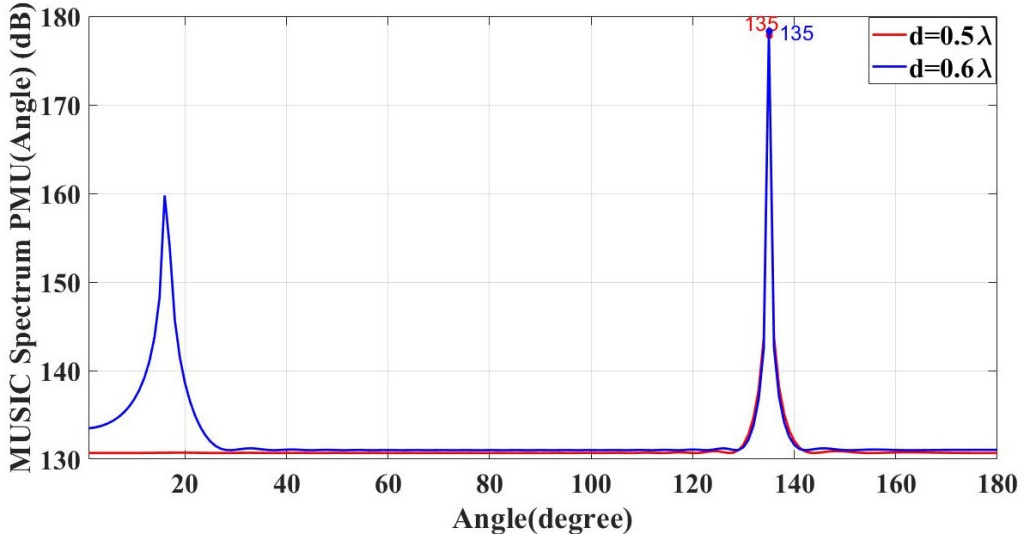
Figure 26: Performance of the MUSIC algorithm for different array spacing

By utilizing equation (56)

$$dmax = \frac{\lambda}{(1 + |cos(135)|)} = 0.6\lambda \tag{58}$$

The results depicted in Fig. 26, in conjunction with Equation (58), provide clear evidence that an inter-element spacing of 0.6λ for the antenna array at a mobile station serves as the critical threshold at which grating lobes start to appear, specifically when the angle of arrival equal 135.

Fig. 27 depicts the inter-element spacing in which grating lobes become apparent at an angle of arrival 90.
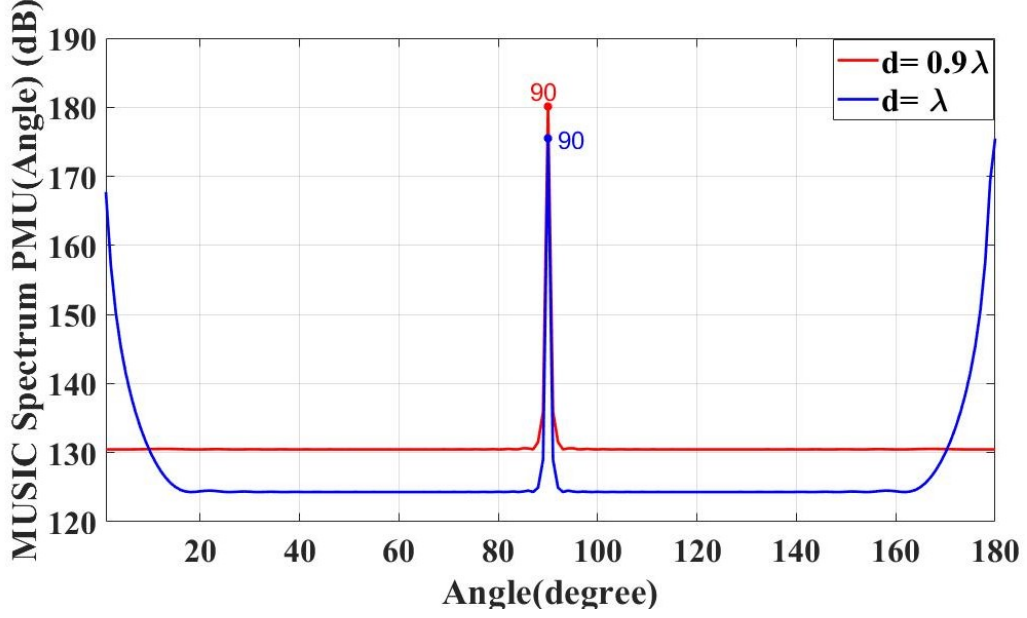
Figure 27: Performance of the MUSIC algorithm for different array spacing

By utilizing equation (56)

$$dmax = \frac{\lambda}{(1 + |cos(90)|)} = \lambda \tag{59}$$

The findings illustrated in Fig. 27, in combination with Equation (59), indicate that when the Angle of Arrival at the mobile station equals 90 degrees, the critical threshold for the inter-element spacing at which grating lobes start to appear is λ.

By examining these additional examples and applying the same law, we can evaluate the effectiveness and reliability of the equation (56) in predicting the onset of grating lobes.

Fig. 28 showcases the angle of arrival estimation results using MUSIC and MIN-NORM algorithms when the inter-element spacing in the array antenna is set to 0.5 λ. The results demonstrate the high accuracy of both algorithms in estimating the arrival angle of the received signal at the mobile station. The MUSIC technique demonstrates better performance compared to the MIN-NORM technique, characterized by its narrower beam width and absence of minor peaks.
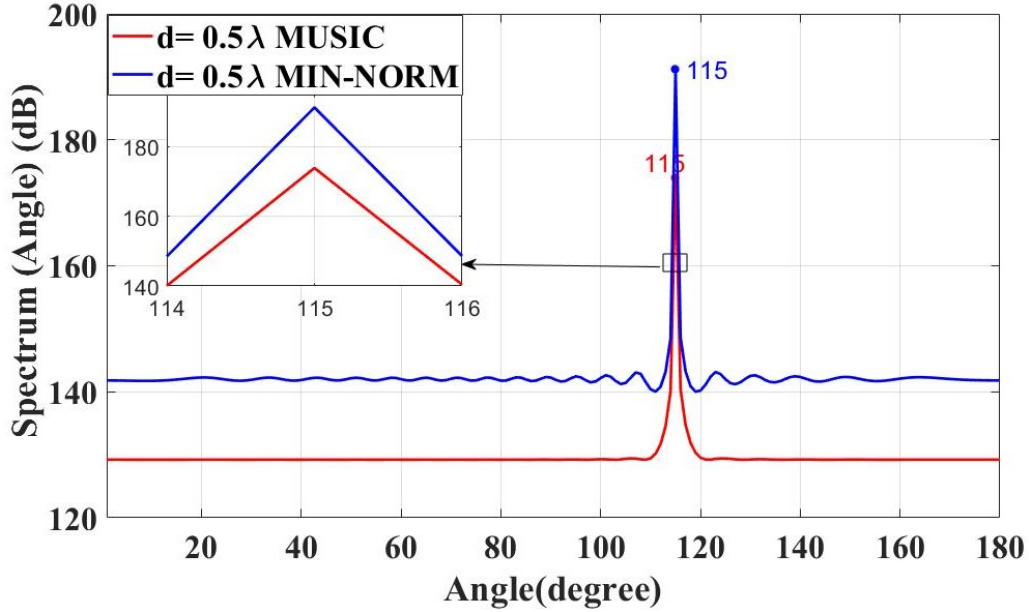
Figure 28: The performance of the MUSIC and MIN-NORM algorithms when (Nm = 20, T = 500, Nr = 200, $\eta = 2, Ps = 1 watt, d = \lambda/2$).

Fig. 29 depicts the RMSE results of the angle of arrival estimation in relation to the inter-element spacing between antenna array elements while keeping all other simulation parameters constant. The Monte Carlo estimations were conducted across 100 simulations. Based on the presented results, it can be observed that both algorithms yield an RMSE of 0.017 for any value of the inter-element spacing within the range of 0.1λ to λ. Although grating lobes appeared when the distance between elements was 0.7λ or greater, the sharp peak for the angle of arrival was higher than peak for the grating lobe as shown in Fig. 24 and Fig. 25, thereby not affecting on RMSE. But in other scenarios, it is possible that the sharp peak corresponding to the angle of arrival is smaller than the peak of the grating lobe, resulting in an incorrect estimate of the angle of arrival.
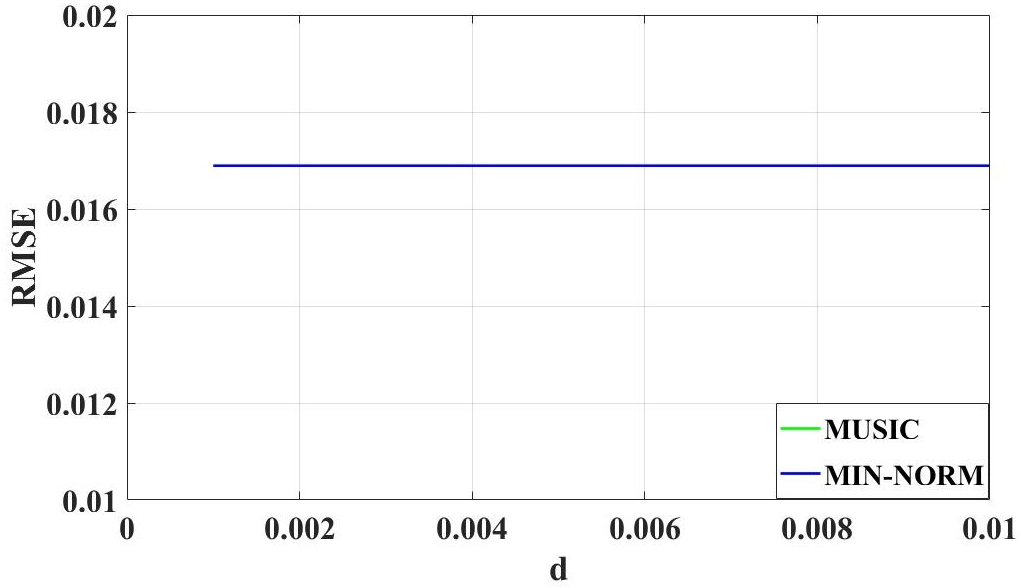
Figure 29: RMSE Versus Inter element spacing when (Nm = 20, T = 500, Nr = 200, $\eta = 2, Ps = 1watt$).

6. Propagation environment.

The path loss exponent is a parameter that defines the propagation environment in wireless communication networks. A lower path loss exponent indicates a more favorable environment for wireless communications, while a higher exponent signifies a more noisy propagation environment. The effect of the path loss exponent on the MUSIC spectrum is shown in Fig. 30, and the impact of the path loss exponent on the MIN-NORM spectrum is depicted in Fig. 31.
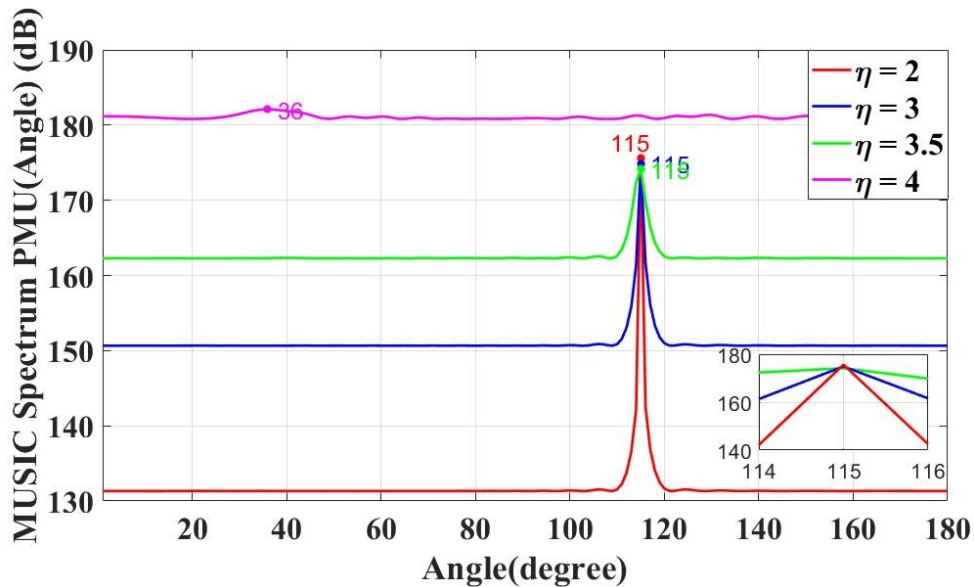
Figure 30: MUSIC algorithm performance for different path loss exponents.
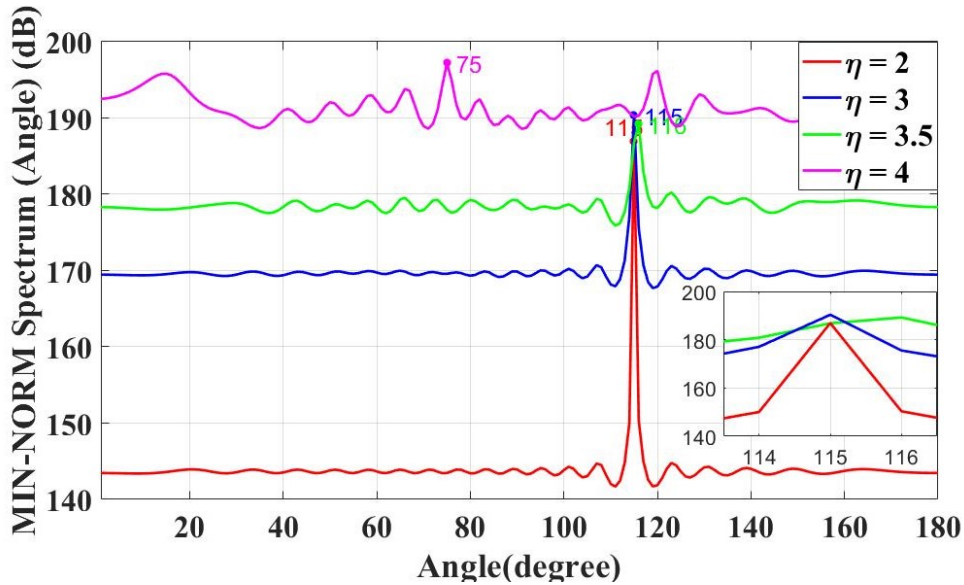
Figure 31: MIN-NORM algorithm performance for different path loss exponents.

Table 6: Received signal power and SNR at the mobile station for different path loss exponent (Nr = 200, Nm = 20, T = 500, d = $\lambda/2$, $Ps = 1Watt$).

η	Pr (dBm)	SNR (dB)
2	-88.5	25.5
3	-113.7	0.30
3.5	-125.6	-11.63
4	-138	-24

The simulated results in Fig. 30 and Fig. 31, along with Table. 6, indicate that the path loss exponent has a direct and negative effect on the performance of the MUSIC algorithm and the MIN-NORM algorithm. As the path loss exponent increases, the power of the received signal decreases, resulting in a decrease in SNR. Additionally, the sharpness of the peak in the MUSIC spectrum and MIN-NORM spectrum decreases, and the beamwidth increases. As a result, the directivity and accuracy of the angle of arrival estimation decrease. We can estimate the angle of arrival using the MUSIC algorithm when the path loss exponent is between 2 and 3.5, and using MIN-NORM when the path loss exponent is between 2 and 3. However, the estimation task becomes more difficult using both algorithms when $\eta = 4$ due to the lower SNR value.

The performance of the angle of arrival estimation algorithms is illustrated in Fig. 32 for a scenario where the path loss exponent is set to 3, while all other parameters remain constant. The results emphasize the MIN-NORM and MUSIC algorithms' accuracy and effectiveness in estimating the arrival angle. Notably, the MUSIC technique outperforms the MIN-NORM technique with its narrower beam width and absence of additional small peaks.
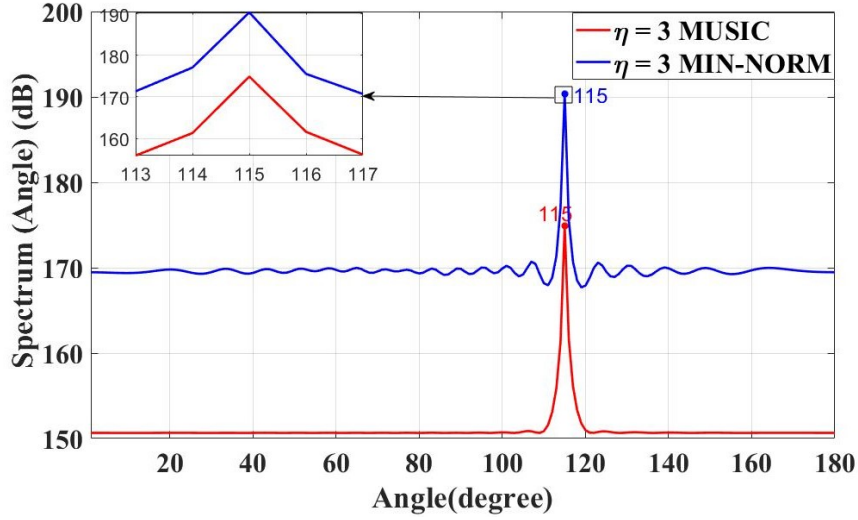
Figure 32: The performance of the MUSIC and MIN-NORM algorithms (when $\eta = 3, Nr = 200, Nm = 20, T = 500, d = \lambda/2, Ps = 1watt$).

Fig. 33 illustrates the RMSE results of the angle of arrival estimation with respect to the path loss exponent. Through conducting 100 Monte Carlo simulations, the results indicate that both the MUSIC and MIN-NORM algorithms perform well within the range of path loss exponent 1.6 to 3.7.
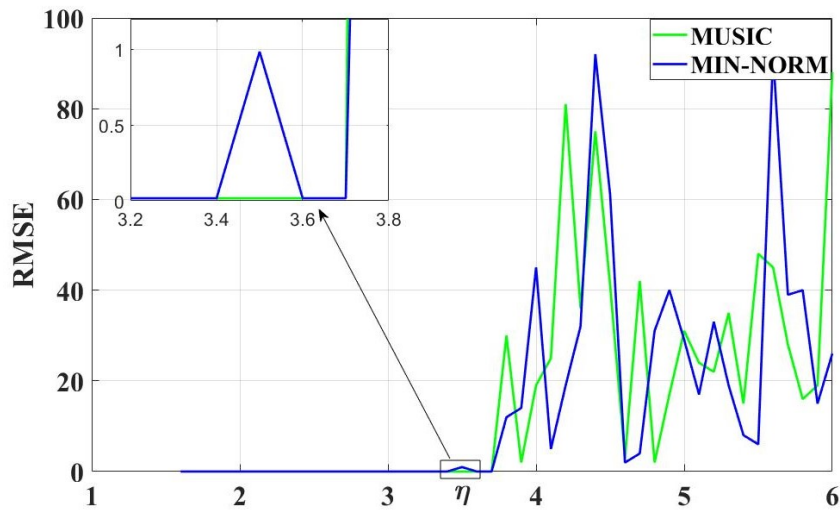
Figure 33: RMSE Versus path loss exponent (when Nr = 200, Nm = 20, T = 500, d = $\lambda/2, Ps = 1watt$).

7. Location of RIS and the mobile station.

In this part, we want to study the effect of the distance between the mobile station and the RIS on the angle of arrival estimation accuracy. The location of the base station and the RIS is fixed, with the distance between them being 18m, and the location of the mobile station is variable. Then, we present the results in Fig. 34 and Fig. 35 and Table. 7

Figure 34: Performance of the MUSIC algorithm at different locations for the mobile station when the distance from BS to RIS = 18 m.

Figure 35: Performance of the MUSIC algorithm at different locations for the mobile station when the distance from BS to RIS = 18 m.

Table 7: The received signal power and SNR at the mobile station for different locations($\eta = 2, Nm = 20, Nr = 200, T = 500, P_s = 1watt, d = \lambda/2$, distance BS - RIS = 18 m).

Distance between RIS-MS	Pr(dBm)	SNR(dB)	True AoA2	Estimated AoA2
15m	-87.96	26.03	90	90
35m	-94.37	19.62	154.86	154.9
45m	-96.49	17.51	160.56	160.6
50m	-97.44	16.7	162.65	162.7
100m	-103.418	9.8	171.38	171.6
200m	-109.52	3.87	175.69	176.4

The simulated results of Fig. 34 and Fig. 35 and Table. 7 indicate that, as the distance between the RIS and the mobile station increases, the power of the received signal at the mobile station decreases, the SNR decreases, the sharpness of the peak in the MUSIC spectrum decreases, and the directivity decreases, thus reducing the accuracy of the estimation angle of arrival of the received signal at the mobile.

In this scenario, to obtain an accurate estimation of the angle of arrival, it is necessary to ensure that the distance between the RIS and the mobile station is less than 100m.

In this part of the study, the distance between the base station and the RIS will be increased to 100 meters while keeping all other simulation parameters constant. Then, we want to study the effect of the change in distance between the mobile station and the RIS on the accuracy of the angle-of-arrival estimation.
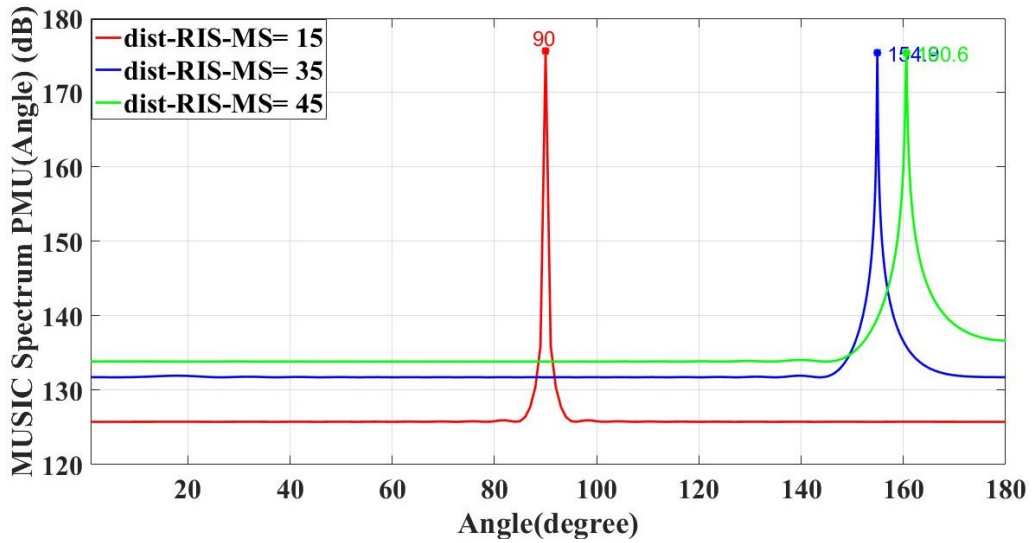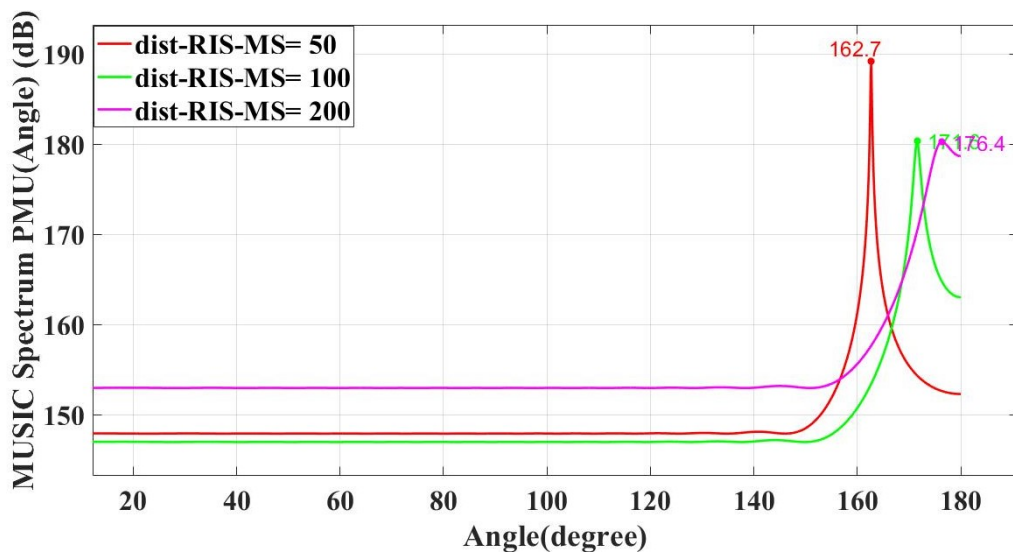

Figure 36: Performance of the MUSIC algorithm at different locations for the mobile station when the distance from BS to RIS = 100 m.

Table 8: The received signal power and SNR at different locations for the mobile station when the distance from BS to RIS = 100 m ($\eta = 2, Nm = 20, Nr = 200, T = 500, Ps = 1 watt$).

Distance between RIS-MS	Pr(dBm)	SNR(dB)	True AoA2	Estimated AoA2
15m	-102.2	11.8	90	90
50m	-113.46	0.54	163.3	163.4
100m	-119.2	-5.2	171.5	172.4

The simulation results of Fig. 36 and Table. 8 indicate that, when the distance between the base station and the RIS was increased to 100 m and the distance between the RIS and the mobile station increased, the path loss effect increased, the power of the received signal at the mobile station decreased, the SNR decreased, the peak sharpness of the MUSIC spectrum decreased, and the directivity decreased, resulting in a reduction of the accuracy of the estimated angle of arrival of the received signal at the mobile. In this scenario, to obtain an accurate estimation of the angle of arrival, it is necessary to ensure that the distance between the RIS and the mobile station is less than 50m.

In this part, we want to increase the distance between the base station and the RIS to 500m. Then, we want to study the effect of the change in distance between the mobile station and the RIS on the accuracy of the angle-of-arrival estimation.
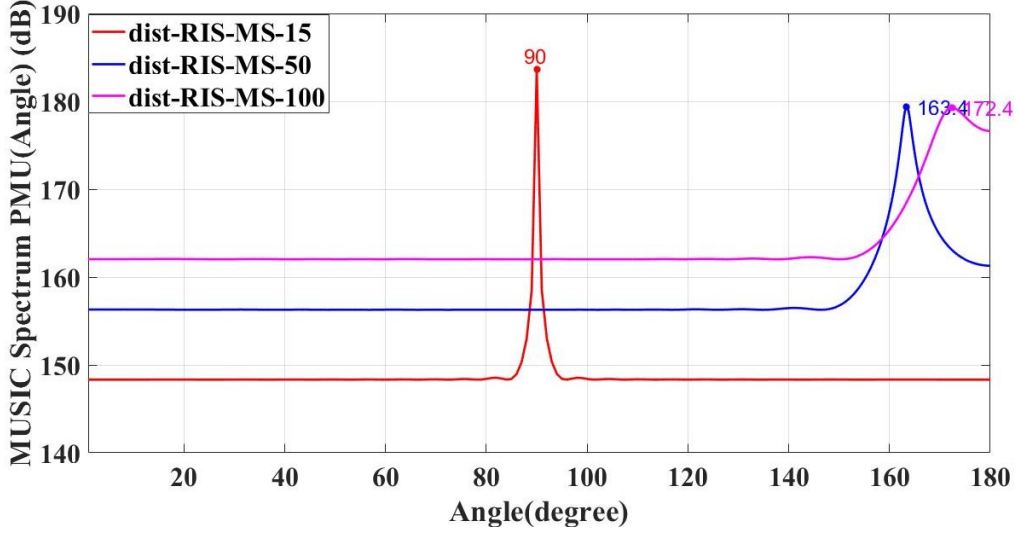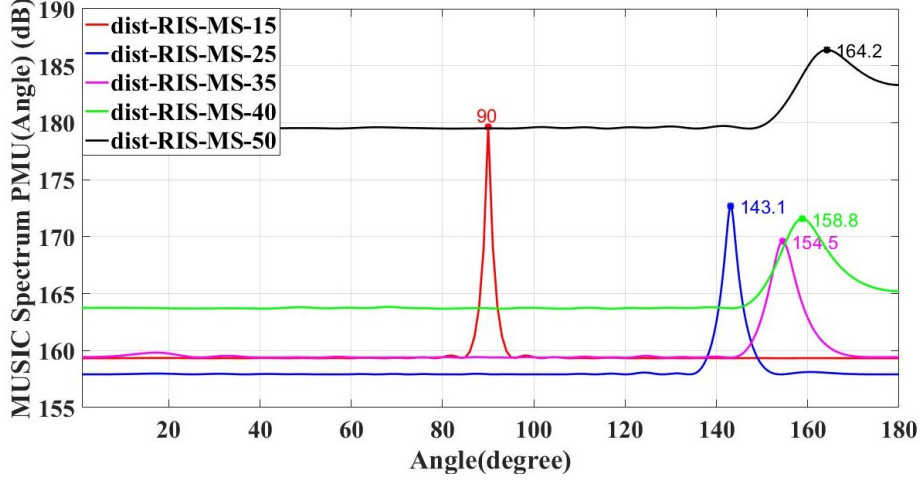

Figure 37: Performance of the MUSIC algorithm at different locations for the mobile station when the distance from BS to RIS = 500 m.

Table 9: The received signal power and SNR at different locations for the mobile station when the distance from BS to RIS = 500 m ($\eta = 2, Nm = 20, Nr = 200, T = 500, Ps = 1watt$).

Distance between RIS-MS	Pr(dBm)	SNR(dB)	True AoA2	Estimated AoA2
15m	-116.5	-2.5	90	90
25m	-120.63	-6.63	143.13	143.1
35m	-124.4	-10.4	154.89	154.5
40m	-125.14	-11.14	157.93	158.8
50m	-127.28	-13.28	162.65	164.2

The simulation results of Fig. 37 and Table. 9 indicate that, when the distance between the base station and the RIS was increased to 500 m and the distance between the RIS and the mobile station increased, the path loss effect increased, the power of the received signal at the mobile station decreased, the SNR decreased, the peak sharpness of the MUSIC spectrum decreased, and the directivity decreased, resulting in a reduction of the accuracy of the estimated angle of arrival of the received signal at the mobile. In this case, the distance between the RIS and the mobile station is limited to a maximum of 25 m.

Consequently, it is important to position the RIS at a moderate distance from the base station to ensure optimum coverage, increase the received signal strength at the mobile station, and minimize errors in angle detection.

9 Conclusion

This thesis presents angle-of-arrival estimation using the MUSIC and MIN-NORM algorithms. Both algorithms exhibit good performance in accurately estimating the angle of arrival. The MUSIC algorithm outperforms the MIN-NORM algorithm with its narrower beam width and absence of additional small peaks. While the MIN-NORM algorithm generates small other peaks in some locations, limiting its efficiency, small peaks gradually disappear from the MIN-Norm spectrum when increasing the number of array elements at the mobile station. The simulation results indicate that the performance of MUSIC and MIN-NORM algorithms improve with an increase in the number of array elements at the mobile station and RIS, a greater number of snapshots of signals, positioning the RIS at a moderate distance from the base station, an increase in SNR, and increased inter-element spacing of the antenna array. However, it is essential to ensure that the inter-element spacing of the array does not exceed 0.6λ to prevent the appearance of grating lobes. These improvements are analyzed in terms of sharper peaks, narrower beam widths in the MUSIC and MIN-NORM spectra, a clearer and higher resolution of the direction of arrival spectrum with a needle-like peak, and smaller errors in angle detection.

10 Future Work

There are several suggestions for future research, including:

- Using active RIS instead of passive RIS and studying its impact on angle-of-arrival estimation and SNR in different propagation environments. Active RIS involves utilizing elements that reflect the incident signal and amplify it, in contrast to passive RIS, which only reflects the signal with an adjustable phase shift.

- Considering the representation of the RIS as a uniform planar array (UPA) instead of a uniform linear array. Then, evaluate the impact of the RIS shape and size on the accuracy of angle estimation in different propagation environments.

- proposes using multiple RISs simultaneously and examining their effects on communication quality and accuracy. Then, investigate how the presence of multiple RISs can be leveraged to improve angle-of-arrival estimation and communication performance in different propagation environments.

11 Appendix

A Finding the value of ϕ_i

When the transmitted signal from BS impinges on a surface of RIS that consists of a linear array of reflecting elements from a direction AoA1, the signal arrives at each array element and encounters a propagation delay as it travels across the array, as shown in Fig. 38,
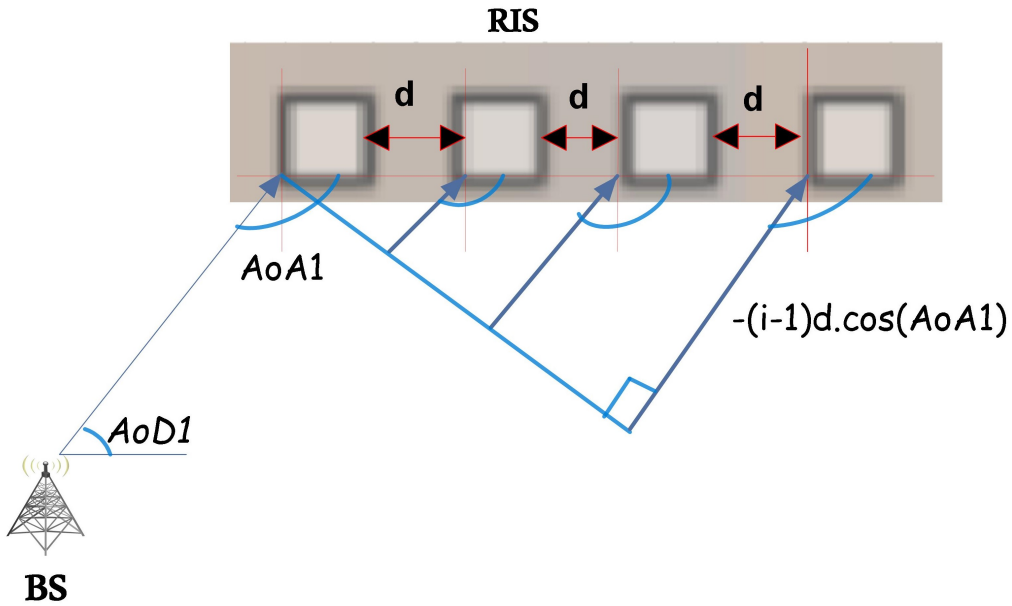
Figure 38: Direction for signal arrival from the BS to the RIS.

The extra distance traveled at element i is equal to (i-1).d.cos(AoD1)= -(i-1).d.cos(AoA1), where d is the distance between any two successive reflector elements, usually set to half-wavelength ($\lambda/2$) at the carrier frequency(f_c). AoD1 denotes the angle of departure (AoD) or direction of departure (DoD) of the transmitted signal from the BS to the RIS is defined at the BS to the horizontal direction, as illustrated in Fig. 2.

To calculate the time delay of arrival signal from BS at the i-th element at RIS denoted by τ_{1i}

$$\tau_{1i} = \frac{distance}{c}$$

$$= \frac{-(i-1).d.cos(AoA1)}{c} \tag{60}$$

$$= \frac{-(i-1).d.cos(AoA1)}{\lambda.f_c}$$

Where c denotes the speed of light.

The direction of the arrival signal from BS to each element on the RIS is

$$\phi_i = 2\pi.f_c.\tau_{1i}$$

$$= -2\pi.f_c.\frac{(i-1).d.cos(AoA1)}{\lambda.f_c} \tag{61}$$

$$= -2\pi.(i-1).\frac{d}{\lambda}.cos(AoA1) \qquad i = 1, 2, \cdots, N.$$

B   Determining the value of φ_k

The signal will be sent from each element on the RIS and arrive at each antenna on the MS with a specific delay, When the signal arrives at MS from RIS, the additional distance traveled at element k at MS is equal to -(k-1).d.cos(AoA2), as shown in Fig. 39,

.
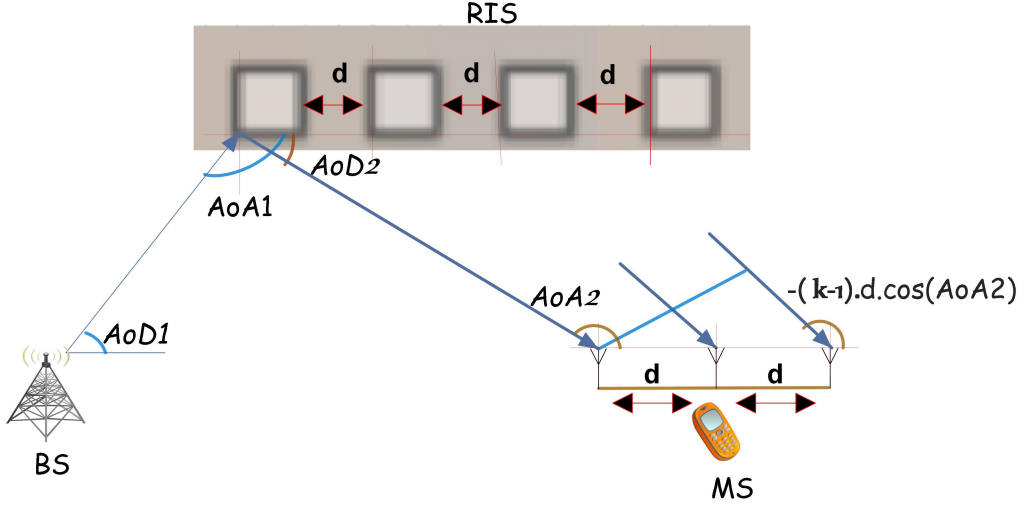
Figure 39:   A uniform linear array antenna with Nm elements.

To calculate the time delay of the arrival signal from the i-th element at the RIS to the MS, it is denoted by τ_{3k} and given by the equation:

$$\tau_{3k} = \frac{-(k-1).d.cos(AoA2)}{\lambda.f_c}. \tag{62}$$

The direction of the arriving signal from RIS is

$$\varphi_k = 2\pi.f_c.\tau_{3k}$$

$$\tag{63}$$

$$= -2\pi.(k-1).\frac{d}{\lambda}.cos(AoA2) \qquad k = 1, 2, \cdots, Nm.$$

C Deriving the value of θ_i

When the signal departs from RIS toward MS, the extra distance traveled at element i is equal to -(i-1).d.cos(AoD2), as shown in Fig. 40.

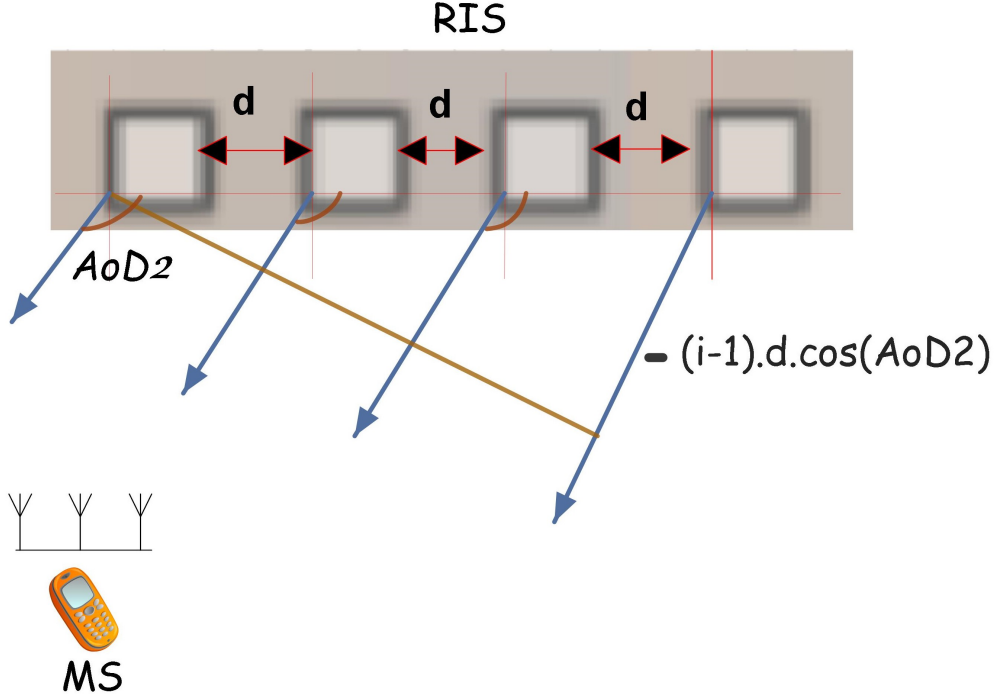Figure 40:   Directional departure signal from the RIS to the MS.

To calculate the time delay departure signal from the i-th element at RIS toward MS denoted by

$$\tau_{2i} = \frac{distance}{c}$$

$$= \frac{-(i-1).d.cos(AoD2)}{\lambda.f_c}.$$

(64)

The direction of the departure signal from RIS is

$$\theta_i = 2\pi.f_c.\tau_{2i}$$

$$= -2\pi.(i-1).\frac{d}{\lambda}.cos(AoD2) \qquad i = 1, 2, \cdots, Nr.$$

(65)

References

[1] M. Mohanna, M. L. Rabeh, E. M. Zieur, S. Hekala, Optimization of music algorithm for angle of arrival estimation in wireless communications, NRIAG journal of Astronomy and Geophysics 2 (1) (2013) 116–124.

[2] J. Miranda, R. Abrishambaf, T. Gomes, P. Gonçalves, J. Cabral, A. Tavares, J. Monteiro, Path loss exponent analysis in wireless sensor networks: Experimental evaluation, in: 2013 11th IEEE international conference on industrial informatics (INDIN), IEEE, 2013, pp. 54–58.

[3] A. Puglielli, N. Narevsky, P. Lu, T. Courtade, G. Wright, B. Nikolic, E. Alon, A scalable massive mimo array architecture based on common modules, in: 2015 IEEE International Conference on Communication Workshop (ICCW), 2015, pp. 1310–1315. doi:10.1109/ICCW.2015.7247359.

[4] S. Hu, F. Rusek, O. Edfors, Beyond massive mimo: The potential of data transmission with large intelligent surfaces, IEEE Transactions on Signal Processing 66 (10) (2018) 2746–2758. doi:10.1109/TSP.2018.2816577.

[5] E. Basar, M. Di Renzo, J. De Rosny, M. Debbah, M. Alouini, R. Zhang, Wireless communications through reconfigurable intelligent surfaces, IEEE Access 7 (2019) 116753–116773. doi:10.1109/ACCESS.2019.2935192.

[6] C. Huang, A. Zappone, G. C. Alexandropoulos, M. Debbah, C. Yuen, Reconfigurable intelligent surfaces for energy efficiency in wireless communication, IEEE Transactions on Wireless Communications 18 (8) (2019) 4157–4170. doi:10.1109/TWC.2019.2922609.

[7] J. He, M. Leinonen, H. Wymeersch, M. Juntti, Channel estimation for ris-aided mmwave mimo channels (2020). arXiv:2002.06453.

[8] Q. Wu, S. Zhang, B. Zheng, C. You, R. Zhang, Intelligent reflecting surface-aided wireless communications: A tutorial, IEEE Transactions on Communications 69 (5) (2021) 3313–3351. doi:10.1109/TCOMM.2021.3051897.

[9] M. Cui, G. Zhang, R. Zhang, Secure wireless communication via intelligent reflecting surface, IEEE Wireless Communications Letters 8 (5) (2019) 1410–1414. doi:10.1109/LWC.2019.2919685.

[10] A. Taha, M. Alrabeiah, A. Alkhateeb, Enabling large intelligent surfaces with compressive sensing and deep learning (2019). arXiv:1904.10136.

[11] Q. Wu, R. Zhang, Intelligent reflecting surface enhanced wireless network via joint active and passive beamforming, IEEE Transactions on Wireless Communications 18 (11) (2019) 5394–5409. doi:10.1109/TWC.2019.2936025.

[12] H. Wymeersch, J. He, B. Denis, A. Clemente, M. Juntti, Radio localization and mapping with reconfigurable intelligent surfaces: Challenges, opportunities, and research directions, IEEE Vehicular Technology Magazine 15 (4) (2020) 52–61. doi:10.1109/MVT.2020.3023682.

[13] J. He, H. Wymeersch, T. Sanguanpuak, O. Silven, M. Juntti, Adaptive beamforming design for mmwave ris-aided joint localization and communication, in: 2020 IEEE Wireless Communications and Networking Conference Workshops (WCNCW), 2020, pp. 1–6. doi:10.1109/WCNCW48565.2020.9124848.

[14] Q.-U.-A. Nadeem, A. Kammoun, A. Chaaban, M. Debbah, M.-S. Alouini, Asymptotic max-min sinr analysis of reconfigurable intelligent surface assisted miso systems, IEEE Transactions on Wireless Communications 19 (12) (2020) 7748–7764. doi:10.1109/TWC.2020.2986438.

[15] M. Jung, W. Saad, Y. Jang, G. Kong, S. Choi, Performance analysis of large intelligent surfaces (liss): Asymptotic data rate and channel hardening effects, IEEE Transactions on Wireless Communications 19 (3) (2020) 2052–2065. doi:10.1109/TWC.2019.2961990.

[16] X. Tan, Z. Sun, D. Koutsonikolas, J. M. Jornet, Enabling indoor mobile millimeter-wave networks based on smart reflect-arrays, in: IEEE INFOCOM 2018 - IEEE Conference on Computer Communications, 2018, pp. 270–278. doi:10.1109/INFOCOM.2018.8485924.

[17] E. Basar, Reconfigurable intelligent surface-based index modulation: A new beyond mimo paradigm for 6g, IEEE Transactions on Communications 68 (5) (2020) 3187–3196. doi:10.1109/TCOMM.2020.2971486.

[18] B. C. Nguyen, T. M. Hoang, P. T. Tran, T. N. Nguyen, V.-D. Phan, B. V. Minh, M. Voznak, Cooperative communications for improving the performance of bidirectional full-duplex system with multiple reconfigurable intelligent surfaces, IEEE Access 9 (2021) 134733–134742. doi:10.1109/ACCESS.2021.3114713.

[19] S. Zeng, H. Zhang, B. Di, Z. Han, L. Song, Reconfigurable intelligent surface (ris) assisted wireless coverage extension: Ris orientation and location optimization, IEEE Communications Letters 25 (1) (2021) 269–273. doi:10.1109/LCOMM.2020.3025345.

[20] L. Yang, Y. Yang, M. O. Hasna, M.-S. Alouini, Coverage, probability of snr gain, and dor analysis of ris-aided communication systems, IEEE Wireless Communications Letters 9 (8) (2020) 1268–1272. doi:10.1109/LWC.2020.2987798.

[21] D. Li, Ergodic capacity of intelligent reflecting surface-assisted communication systems with phase errors, IEEE Communications Letters 24 (8) (2020) 1646–1650. doi:10.1109/LCOMM.2020.2997027.

[22] C. Guo, Y. Cui, F. Yang, L. Ding, Outage probability analysis and minimization in intelligent reflecting surface-assisted miso systems, IEEE Communications Letters 24 (7) (2020) 1563–1567. doi:10.1109/LCOMM.2020.2975182.

[23] M.-A. Badiu, J. P. Coon, Communication through a large reflecting surface with phase errors, IEEE Wireless Communications Letters 9 (2) (2020) 184–188. doi:10.1109/LWC.2019.2947445.

[24] H. Zhang, B. Di, L. Song, Z. Han, Reconfigurable intelligent surfaces assisted communications with limited phase shifts: How many phase shifts are enough?, IEEE Transactions on Vehicular Technology 69 (4) (2020) 4498–4502. doi:10.1109/TVT.2020.2973073.

[25] P. Xu, G. Chen, Z. Yang, M. D. Renzo, Reconfigurable intelligent surfaces-assisted communications with discrete phase shifts: How many quantization levels are required to achieve full diversity?, IEEE Wireless Communications Letters 10 (2) (2021) 358–362. doi:10.1109/LWC.2020.3031084.

[26] X. Qian, M. Di Renzo, J. Liu, A. Kammoun, M.-S. Alouini, Beamforming through reconfigurable intelligent surfaces in single-user mimo systems: Snr distribution and scaling laws in the presence of channel fading and phase noise, IEEE Wireless Communications Letters 10 (1) (2021) 77–81. doi:10.1109/LWC.2020.3021058.

[27] Q. Wu, R. Zhang, Beamforming optimization for wireless network aided by intelligent reflecting surface with discrete phase shifts, IEEE Transactions on Communications 68 (3) (2020) 1838–1851. doi:10.1109/TCOMM.2019.2958916.

[28] B. Di, H. Zhang, L. Li, L. Song, Y. Li, Z. Han, Practical hybrid beamforming with finite-resolution phase shifters for reconfigurable intelligent surface based multi-user communications, IEEE Transactions on Vehicular Technology 69 (4) (2020) 4565–4570. doi:10.1109/TVT.2020.2973202.

[29] C. Huang, S. Hu, G. C. Alexandropoulos, A. Zappone, C. Yuen, R. Zhang, M. D. Renzo, M. Debbah, Holographic mimo surfaces for 6g wireless networks: Opportunities, challenges, and trends, IEEE Wireless Communications 27 (5) (2020) 118–125. doi:10.1109/MWC.001.1900534.

[30] H. Shen, W. Xu, S. Gong, Z. He, C. Zhao, Secrecy rate maximization for intelligent reflecting surface assisted multi-antenna communications, IEEE Communications Letters 23 (9) (2019) 1488–1492. doi:10.1109/LCOMM.2019.2924214.

[31] N. S. Perović, M. D. Renzo, M. F. Flanagan, Channel capacity optimization using reconfigurable intelligent surfaces in indoor mmwave environments, in: ICC 2020 - 2020 IEEE International Conference on Communications (ICC), 2020, pp. 1–7. doi:10.1109/ICC40277.2020.9148781.

[32] L. Yang, Y. Yang, D. B. da Costa, I. Trigui, Outage probability and capacity scaling law of multiple ris-aided cooperative networks (2020). arXiv:2007.13293.

[33] S. Li, B. Duo, X. Yuan, Y.-C. Liang, M. Di Renzo, Reconfigurable intelligent surface assisted uav communication: Joint trajectory design and passive beamforming, IEEE Wireless Communications Letters 9 (5) (2020) 716–720.

[34] M. Hua, L. Yang, Q. Wu, C. Pan, C. Li, A. L. Swindlehurst, Uav-assisted intelligent reflecting surface symbiotic radio system, IEEE Transactions on Wireless Communications 20 (9) (2021) 5769–5785.

[35] L. Wang, K. Wang, C. Pan, N. Aslam, Joint trajectory and passive beamforming design for intelligent reflecting surface-aided uav communications: A deep reinforcement learning approach, IEEE Transactions on Mobile Computing.

[36] M. Shehata, M. Crussière, M. Hélard, On the theoretical limits of beam steering in mmwave massive mimo channels, in: 2019 IEEE 30th Annual International Symposium on Personal, Indoor and Mobile Radio Communications (PIMRC), 2019, pp. 1–6.

[37] W. Diego, J. Kelif, Improving d2d communications using 3d beamforming in 5g wireless networks, in: 2017 IEEE 28th Annual International Symposium on Personal, Indoor, and Mobile Radio Communications (PIMRC), 2017, pp. 1–6.

[38] C. A. Balanis, P. I. Ioannides, Introduction to smart antennas, Synthesis Lectures on Antennas 2 (1) (2007) 1–175.

[39] M. Zhou, X. Zhang, X. Qiu, C. Wang, Two-dimensional doa estimation for uniform rectangular array using reduced-dimension propagator method, International Journal of Antennas and Propagation 2015 (2015).

[40] F. B. Gross, Smart antennas with MATLAB®, McGraw-Hill Education, 2015.

[41] W. Zhang, W. Zhang, Beam training and tracking efficiency analysis for uav mmwave communication, in: 2018 IEEE International Conference on Communication Systems (ICCS), 2018, pp. 115–119.

[42] S. Kim, H. Han, N. Kim, H. Park, Robust beam tracking algorithm for mmwave mimo systems in mobile environments, in: 2019 IEEE 90th Vehicular Technology Conference (VTC2019-Fall), 2019, pp. 1–5.

[43] S. Jayaprakasam, X. Ma, J. W. Choi, S. Kim, Robust beam-tracking for mmwave mobile communications, IEEE Communications Letters 21 (12) (2017) 2654–2657.

[44] A. Badawy, T. Khattab, D. Trinchero, T. M. Elfouly, A. Mohamed, A simple aoa estimation scheme, ArXiv abs/1409.5744 (2014).

[45] Z. Chen, G. Gokeda, Y. Yu, Introduction to Direction-of-arrival Estimation, Artech House, 2010.

[46] J. Capon, High-resolution frequency-wavenumber spectrum analysis, Proceedings of the IEEE 57 (8) (1969) 1408–1418. doi:10.1109/PROC.1969.7278.

[47] J. Li, P. Stoica, Z. Wang, On robust capon beamforming and diagonal loading, IEEE transactions on signal processing 51 (7) (2003) 1702–1715.

[48] M. Mohanna, M. L. Rabeh, E. M. Zieur, S. Hekala, Optimization of music algorithm for angle of arrival estimation in wireless communications, NRIAG Journal of Astronomy and Geophysics 2 (1) (2013) 116–124. arXiv:https://doi.org/10.1016/j.nrjag.2013.06.014, doi:10.1016/j.nrjag.2013.06.014.
URL https://doi.org/10.1016/j.nrjag.2013.06.014

[49] M. M. Gunjal, A. B. Raj, Improved direction of arrival estimation using modified music algorithm, in: 2020 5th International Conference on Communication and Electronics Systems (ICCES), 2020, pp. 249–254. doi:10.1109/ICCES48766.2020.9137982.

[50] P. Laxmikanth, S. Susruthababu, L. Surendra, S. S. Babu, D. V. Ratnam, Enhancing the performance of aoa estimation in wireless communication using the music algorithm, in: 2015 International Conference on Signal Processing and Communication Engineering Systems, 2015, pp. 448–452. doi:10.1109/SPACES.2015.7058304.

[51] T. N. Rao, V. Rao, Evaluation of music algorithm for a smart antenna system for mobile communications, in: 2012 International Conference on Devices, Circuits and Systems (ICDCS), 2012, pp. 67–71. doi:10.1109/ICDCSyst.2012.6188676.

[52] L. Godara, Application of antenna arrays to mobile communications. ii. beam-forming and direction-of-arrival considerations, Proceedings of the IEEE 85 (8) (1997) 1195–1245. doi:10.1109/5.622504.

[53] Z. Wei, X. Xiaoli, Analysis and simulation of the direction of arrival estimation algorithm of spatial signal, in: 2007 8th International Conference on Electronic Measurement and Instruments, 2007, pp. 2–576–2–579. doi:10.1109/ICEMI.2007.4350746.

[54] A. Naceur, Improving the resolution performance of min-norm and root-min-norm algorithms for adaptive array antenna, in: 2017 5th International Conference on Electrical Engineering - Boumerdes (ICEE-B), 2017, pp. 1–5. doi:10.1109/ICEE-B.2017.8191987.

[55] P. Gupta, V. K. Verma, V. Senapati, Angle of arrival detection by esprit method, in: 2017 International Conference on Communication and Signal Processing (ICCSP), 2017, pp. 1143–1147.

[56] G. Zheng, B. Chen, M. Yang, Unitary esprit algorithm for bistatic mimo radar, Electronics Letters 48 (3) (2012) 179–181.

[57] C.-B. Ko, J.-H. Lee, Performance of esprit and root-music for angle-of-arrival(aoa) estimation, in: 2018 IEEE World Symposium on Communication Engineering (WSCE), 2018, pp. 49–53. doi:10.1109/WSCE.2018.8690541.

[58] Z. jaafer, S. Goli, A. S. Elameer, Performance analysis of beam scan, min-norm, music and mvdr doa estimation algorithms, in: 2018 International Conference on Engineering Technology and their Applications (IICETA), 2018, pp. 72–76. doi:10.1109/IICETA.2018.8458076.

[59] P. Gupta, K. Aditya, A. Datta, Comparison of conventional and subspace based algorithms to estimate direction of arrival (doa), in: 2016 International Conference on Communication and Signal Processing (ICCSP), 2016, pp. 0251–0255. doi:10.1109/ICCSP.2016.7754133.

[60] F. Li, H. Liu, R. J. Vaccaro, Performance analysis for doa estimation algorithms: unification, simplification, and observations, IEEE Transactions on Aerospace and Electronic Systems 29 (4) (1993) 1170–1184.

[61] O. A. Oumar, M. F. Siyau, T. P. Sattar, Comparison between music and esprit direction of arrival estimation algorithms for wireless communication systems, in: The First International Conference on Future Generation Communication Technologies, 2012, pp. 99–103. doi:10.1109/FGCT.2012.6476563.

[62] M. Gavish, A. Weiss, Performance analysis of the via-esprit algorithm, in: IEE Proceedings F (Radar and Signal Processing), Vol. 140, IET, 1993, pp. 123–128.

[63] J. Sanson, A. Gameiro, D. Castanheira, P. P. Monteiro, Comparison of doa algorithms for mimo ofdm radar, in: 2018 15th European Radar Conference (EuRAD), 2018, pp. 226–229. doi:10.23919/EuRAD.2018.8546582.

[64] Y. S. Cho, J. Kim, W. Y. Yang, C. G. Kang, The Wireless Channel: Propagation and Fading, 2010, pp. 1–24. doi:10.1002/9780470825631.ch1.

[65] T. Rappaport, Wireless communications: Principles and practice, 2nd Edition, Prentice Hall communications engineering and emerging technologies series, Prentice Hall, 2002, includes bibliographical references and index.

[66] J. G. Proakis, M. Salehi, Digital communications, Vol. 4, McGraw-hill New York, 2001.

[67] Wireless Communications: Principles and Practice, 2e, Prentice Hall PTR, 1996.
URL https://books.google.ps/books?id=gPKODwAAQBAJ

[68] Y. S. Cho, J. Kim, W. Y. Yang, C. G. Kang, MIMO-OFDM wireless communications with MATLAB, John Wiley & Sons, 2010.

[69] T. Feng, T. R. Field, Statistical analysis of mobile radio reception: an extension of clarke's model, IEEE Transactions on Communications 56 (12) (2008) 2007–2012. doi:10.1109/TCOMM.2008.060596.

[70] T. S. Rappaport, Wireless Communications: Principles and Practice, 2nd Edition, 2002.

[71] P. M. Shankar, Fading and shadowing in wireless systems, Springer, 2017.

[72] Z. Liu, Z. Zhu, W. Hao, J. Zhang, Aerial intelligent reflecting surface for secure miso communication systems, in: International Conference on Communications and Networking in China, Springer, 2021, pp. 553–566.

[73] Q. Wu, R. Zhang, Intelligent reflecting surface enhanced wireless network: Joint active and passive beamforming design, in: 2018 IEEE Global Communications Conference (GLOBE-COM), IEEE, 2018, pp. 1–6.

[74] Q. Wu, R. Zhang, Intelligent reflecting surface enhanced wireless network via joint active and passive beamforming, IEEE Transactions on Wireless Communications 18 (11) (2019) 5394–5409.

[75] Q. Wu, R. Zhang, Towards smart and reconfigurable environment: Intelligent reflecting surface aided wireless network, IEEE Communications Magazine 58 (1) (2019) 106–112.

[76] C. Huang, A. Zappone, M. Debbah, C. Yuen, Achievable rate maximization by passive intelligent mirrors, in: 2018 IEEE International Conference on Acoustics, Speech and Signal Processing (ICASSP), 2018, pp. 3714–3718. doi:10.1109/ICASSP.2018.8461496.

[77] P. Gupta, S. Kar, Music and improved music algorithm to estimate direction of arrival, in: 2015 International Conference on Communications and Signal Processing (ICCSP), 2015, pp. 0757–0761. doi:10.1109/ICCSP.2015.7322593.

[78] M. H. Hayes, Statistical digital signal processing and modeling, John Wiley & Sons, 1996.

[79] Z. Iqbal, M. Pour, Grating lobe reduction in scanning phased array antennas with large element spacing, IEEE transactions on antennas and propagation 66 (12) (2018) 6965–6974.